Emergent geometries of groundwater-fed rivers

by

Robert Sngho Yi

Submitted to the Department of Earth, Atmospheric and Planetary Sciences
in partial fulfillment of the requirements for the degree of

Doctor of Philosophy in Geophysics

at the

MASSACHUSETTS INSTITUTE OF TECHNOLOGY

September 2017

Author .....
Department of Earth, Atmospheric and Planetary Sciences
September 8, 2017

Certified by .....
Daniel H. Rothman
Professor
Thesis Supervisor

Accepted by .....
Robert D. van der Hilst
Schlumberger Professor of Earth and Planetary Sciences
Head of the Department

Emergent geometries of groundwater-fed rivers

by

Robert Sngho Yi

Submitted to the Department of Earth, Atmospheric and Planetary Sciences
on September 8, 2017, in partial fulfillment of the
requirements for the degree of
Doctor of Philosophy in Geophysics

Abstract

Groundwater-fed rivers form stunning geometries over a range of scales. These rivers grow as water from an underground aquifer reemerges and erodes the overlying topography. Both the aquifer and the overlying topography generate flows along diffusive gradients. We study three features produced by these gradients over different scales: the shape of the valley that forms around a single stream, the network-averaged planform stream shape, and the shape of the drainage basin. First, we identify a new feature in stream valleys – a spatially variable diffusivity – that gives rise to a theoretical valley shape that agrees with the shapes of real valleys. Next, we present evidence and theory for a 120° opening stream confluence angle as a result of lateral rearrangement of streams in response to the pressure field generated by the aquifer. We then study how this mechanism exerts itself on the scale of the network. Finally, we widen our scope and analyze river planform morphology on a continental scale. We identify how branching angles can predict a river basin aspect ratio. We find a relationship between this aspect ratio and river basin scaling exponents with local climate.

Thesis Supervisor: Daniel H. Rothman
Title: Professor

Acknowledgments

Thank you first to Dan for your guidance and generosity throughout the years in spite of my frequent cynicism, petulance, and verbosity. Thesis work has often felt like random walk, but you made the dimensionality feel more like 2 than 3. Thank you also to my colleagues for hours of interesting conversation – David, Paul, Chris, Yonatan, Haitao, Eric, Yossi, Hans, Sai, Randy, Goody. Thank you to members of my thesis committee – Taylor Perron, David McGee, Olivier Devauchelle – and all others I've had the chance to work with for building my scientific taste out of a millenial idealism. Thank you to those at the Nature Conservancy for guidance through the Apalachicola ravines.

Thank you Borin, Hannah, Liz, James, and J.C. for giving me a family here and wonderful adventures over the years. Thank you to my numerous geographically distant friends – Chris, Joony, Erica, Lawrence, Will, Jon, Justin, Jeff, Yun, Andrew, Simon, Tom, Grace, and so many others. Thank you Dave, Esther, and Mrs. & Rev. Lee for welcoming me so warmly into your family. Thank you Matt and Tamiko and Boston Found for your immense moral support and friendship. And thank you to my family all over for your love and support in spite of the distance between us.

Thank you to my mom for your love and support and exceptional parenting over the years. I am eternally grateful for the wonderful initial conditions you've set up for me, without which none of my accomplishments would have been possible. Finally, thank you to my wife, Gloria, for everything. You are why I know there is so much beauty to be found in the universe. (And sorry to everyone else who read that sentence.) And finally, thank you to anyone I've left out – you are all important!

Contents

List of Figures

A brief history of graduate school:

> *"The most beautiful thing we can experience is the mysterious. It is the source of all true art and science."*
>
> - Albert Einstein

> *"... any hypothesis, however absurd, may be useful in science, if it enables a discoverer to conceive things in a new way; but ... when it has served this purpose by luck, it is likely to become an obstacle to further advance."*
>
> - Bertrand Russell,
> A History of Western Philosophy

> *"Your mind is fallible, but becoming mindless will not make you infallible."*
>
> - Ayn Rand, Atlas Shrugged

> *"Maybe I only see a pattern because I've been staring too long. But then again ... maybe I see a pattern because it's there."*
>
> - Donna Tart, The Goldfinch

Preface

Humans have this innate desire to reduce noisy data to concise laws – to *understand*, even when understanding is evasive. And science is perhaps humanity's best attempt to rigorously consummate this desire. It is the most objective description of the universe that we have and at the same time, fundamentally reductionist. The reduction is certainly necessary, but too often, our eagerness leads us to conflate hypothesis with truth, probability with absolute, and we forget that what we have is not a set of absolutes, but glimpses of a theme – *emergence*. Over the next few paragraphs, I will introduce you to this concept and hopefully, shape a thematic lens through which you will read the papers that follow.

For most intents and purposes, truth and heavily supported hypothesis can be considered equivalent. But one would be hard-pressed to find a scientific conjecture that could in good faith be considered truth. Still, we are taught hundreds of "laws" that represent narrow approximations of our universe within scales relevant to humans. We think of Newton's laws as truth, but the Ehrenfest theorem tells us that they are instead a continuum limit that emerges from quantum mechanics. We think of friction coefficients and viscosity and elasticity as precise, measurable material properties, but they are only macroscopic descriptions of particles converting and storing and dissipating energy. While these descriptions are astonishingly predictive (and wonderfully elegant!), they are not stand-alone absolutes, but rather macroscopic descriptions of microscopic behavior.

Or generally, these are what physicists and philosophers would call *emergent properties*: novel structures that arise from the collective interactions between constituent entities. And emergence is not only the basis of science, but of all complexity in the

(a) (b)

Figure 0-1: Examples of emergent complexity. (a) A snowflake. (b) A city.

natural world – and it is emergence that makes our world so interesting. Our world is not a series of boring absolutes – we are not composed of sets of additive, predictable, reversible quantities. Our world is a continuum of bizarre phenomena and patterns being produced by and giving rise to other phenomena and patterns on different scales. The Big Bang did not give rise to a homogeneous lattice of identical particles of identical energies, but a variegated soup of matter (and anti-matter) that interacted and coalesced to produce elements and molecules, physics and art, snowflakes and cities (see Figure 0-1).

As a brief example, consider the now canonical example of sand grains falling on a pile (Bak et al., 1987; Kadanoff et al., 1989). Sand grains, simply conceived, can do one of two things: fall or stick by friction. Their individual behaviors, therefore, can be understood through mechanics. For example, if I drop a sand grain on a flat surface, the grain will fall, hit the surface, and perhaps bounce a bit, but ultimately it will stop moving somewhere near the point where I dropped it as a result of frictional forces acting on it. If I then remove this sand grain and drop a new one, the sand grain would again fall, hit the surface, bounce, and come to rest probably somewhere else reasonably close to the first sand grain. An incredibly tedious experiment would be to do this many, many times and record the position of the sand grain on the surface as a function of distance from the point at which it was dropped. After a semester of mind-numbing work, the undergraduate likely in charge of this experiment would

find that the distribution of final sand grain positions resembles a normal distribution around the point from which the sand was dropped. But instead of removing the sand grain after each drop, consider what would happen if the undergraduate allowed the sand grains to interact, forming a pile. As he builds up the pile, one sand grain at a time, the pile grows until a critical point at which the next sand grain slides down the pile, carrying some other sand grains with it. The pile is now more shallow, and it will take the addition of more sand grains before it avalanches again. The size distribution of these avalanches takes the form of a power law, and these *avalanches* are an example of emergent phenomena. The grains are subject individually only to simple rules by which they stick and fall, yet as a collective, they form avalanches with properties and behavior that seem radically different from the rules that gave rise to them.

I admit this example seemed as mundane to me as it likely does to you at first blush. But this impression is evidence of our innate familiarity with the concept and its astounding ubiquity. Earthquakes, hillside avalanches, and stock market crashes are perhaps the most direct analogues to the sandpile example I have given. But as we will show, emergence can also manifest structurally, producing complex geometric shapes that are a result of, yet decidedly visually different from their constituent components – snowflakes, seashells, river networks. And as I have mentioned, scientific hypotheses, often touted as absolute truths, are our best attempts as scientists to describe emergent properties. Even humanity itself, with all our culture and music and politics and science, can be understood as coming from comparably simple behaviors seen in physics, chemistry, and biology.

In the following chapters, I hope to convince you that rivers form shapes and exhibit statistical properties that make them a rich example of how emergent geometric complexity can appear over a range of scales. All this is to say that this is not a search for truth, as I once thought it was – it is the exploration of a theme.

Chapter 1

Introduction

1.1 Motivation

Consider the drunkard. The magnification factor by which we observe him is of the utmost importance. At the microscopic level, he is a wondrous sack of interacting molecules, working in tandem to create the precise chemical reactions that give rise to life. At the human scale, he has physical traits, social connections, a job, hobbies, a story. Yet, if we observe his motion, we will notice that each step he takes is independent of the last, thanks to his drunken haze, and his motion is not unlike that of a gas molecule bobbing through space.

Within the domain of his movement, let us assume there is an object with which he may collide, causing him to fall down and remain still. If we now allow other drunkards to roam about, such that they also fall down and cease movement upon collision with either the object or other immobilized drunkards, we obtain stunningly beautiful aerial patterns of drunkards as shown in figure 1-1.

This is certainly a contrived example, as you rarely find piles of drunk people in the streets. However, the resulting phenomena is very real, and is known as diffusion-limited aggregation. While *who* each drunkard is and the chemical reactions that comprise him are of interest, the patterns in figure 1-1 will arise independently of the minute details of the drunkard's life. We need only isolate two properties of the drunkard's walk – his random steps and his inertness upon collision – to obtain a

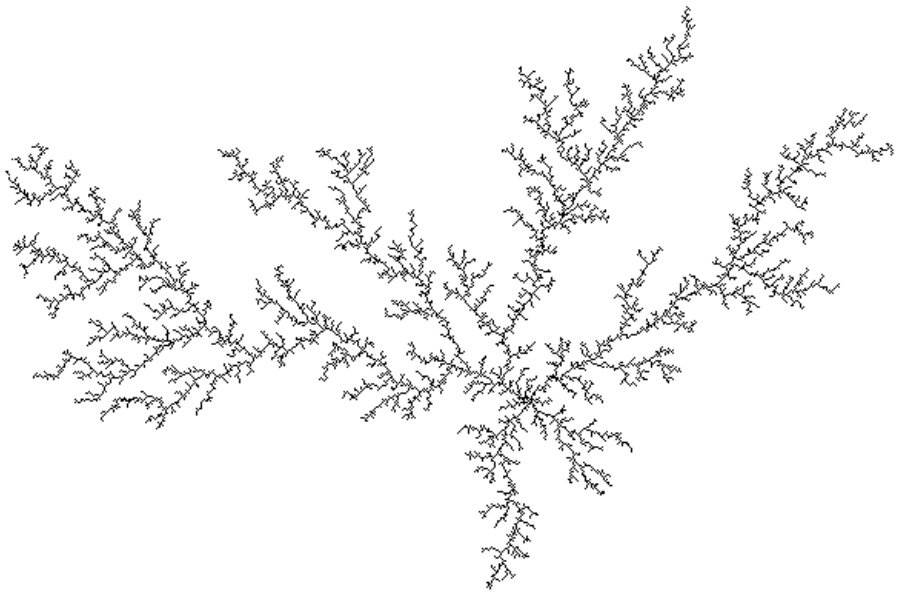

Figure 1-1: A diffusion-limited aggregate.

new, emergent structure.

Rivers are not so different from collections of drunkards in this sense. Rivers are comprised simply of water and some confining substance, such as soil or rock, yet exhibit fascinating structural properties. On the scale of a single river, interactions between soil, rock, and water produce interesting bulk behavior: turbulent, yet predictably helical flow patterns (Rozovskii, 1957; Engelund, 1974) and multiple types of granular transport (Parker, 1990; Houssais et al., 2015). But ultimately, these simple interactions give rise to larger patterns, such as river bends and meanders (Leopold and Wolman, 1960; Einstein, 1926) and junctions (Best, 1988; Devauchelle et al., 2012). At the largest scales, rivers dissect the surface of the Earth, forming highly ramified patterns that do not seem possible from a microscopic study of the water molecule (Montgomery and Dietrich, 1992; Perron et al., 2012).

Unfortunately, while the drunkard can be modelled as a simple random walker, there is no one-size-fits-all model of river pattern formation. Although several simple models of river network formation have been suggested (Scheidegger, 1967; Rodrigeuz-Iturbe and Rinaldo, 1997; Dodds and Rothman, 2000), it is not clear how or when these models should be applied. And fundamentally, the problem is the size of the

variable space we must explore – while the randomness of a particle's movement in conjunction with a sticky boundary are what give rise to the branching pattern in figure 1-1, rivers are subject to a wide number of morphologically important factors on all scales. Rivers can be babbling brooks or rushing rapids (variable size), fed by groundwater flow or overland flow or both, and are subject to all flavors of material, spatial, climatic, biotic, and tectonic forcings (Ritter et al., 2011).

Our approach to the problem will be to break up this variable space and narrow the scope of the problem we study, in the hopes that we will ultimately be able to understand one end of the problem. In particular, we will study a subset of rivers fed by groundwater, and build our understanding from the ground up (literally!). In the remainder of this chapter, I will introduce the reader briefly to the world of groundwater-fed streams. In subsequent chapters, I will explain new features of groundwater-fed rivers that we have found, and ultimately, present results that suggest that our understanding of groundwater-fed streams can inform an understanding of river networks in general.

1.2 Groundwater-fed streams

1.2.1 A song of seepage and soil

The image most readily evoked by "river" is probably a snow-fed, rushing rapid, carving a path down a mountain into a serene, wildlife-laden valley. But these rivers, while beautiful in their own right, have a turbulence and susceptibility to surface inhomogeneities that make their growth difficult to precisely describe mathematically (though, as we will later show, they do exhibit some fascinating, statistically compliant properties). The subset of rivers that we will study herein are arguably less well-advertised, but are subject to more quasistatic growth dynamics, allowing us to predict features of their morphology: groundwater-fed channels. Moreover, their influence on the global hydrological cycle is substantial – 22 to 32% of global land area is affected by groundwater flow (Fan et al., 2013). The advance of these streams

and the valleys that form around them can be understood through two basic physical concepts: groundwater reemergence, which ultimately determines the direction in which the rivers grow, and topographic diffusion, which concerns how the shape of the topography responds to river growth. We will briefly discuss each of these.

Groundwater accumulates as rainfall fills the pore spaces of sediment overlying an impervious boundary, forming an aquifer. When this aquifer reaches a height that exceeds the height of the topography, groundwater is pushed out of the ground by gravity, forming springs. As this groundwater emerges, it carries sediment with it, causing the spring to advance in the direction opposite the direction of water flow. This reemergence, known as *seepage*, forms rivers in a way that is thus primarily a function of how the underground pressure field directs water to the springs. As we will later show, the equations governing this process can be reduced to arguably the simplest and most ubiquitous second-order differential equation: Poisson's equation for the height of the groundwater table squared. This is an equation that, often with only an additional rule or two, can produce wonderfully ramified, fractal patterns. Examples of such patterns are shown in Figure 1-2. While the branching dynamic that produces said fractality in groundwater-fed river networks is different from that which produces lightning, one can at least recognize the auspiciousness of the visual resemblance.

The reason for this difference is the presence of a second process that influences river morphology: topographic diffusion. Seepage can be a very slow process. The springs of the channel network pictured in Figure 1-2 advance at a rate of roughly 1 millimeter per year (Abrams et al., 2009). And over this expansive time scale, processes that seemed otherwise mundane – animals burrowing on hillsides, droplets of rain hitting the ground, light winds that move only a few grains of soil a few millimeters, flora growing and dying – suddenly become important.

> *"The whole surface of the earth seemed changed, melting and flowing under my eyes."*
>
> - H.G. Wells, The Time Machine

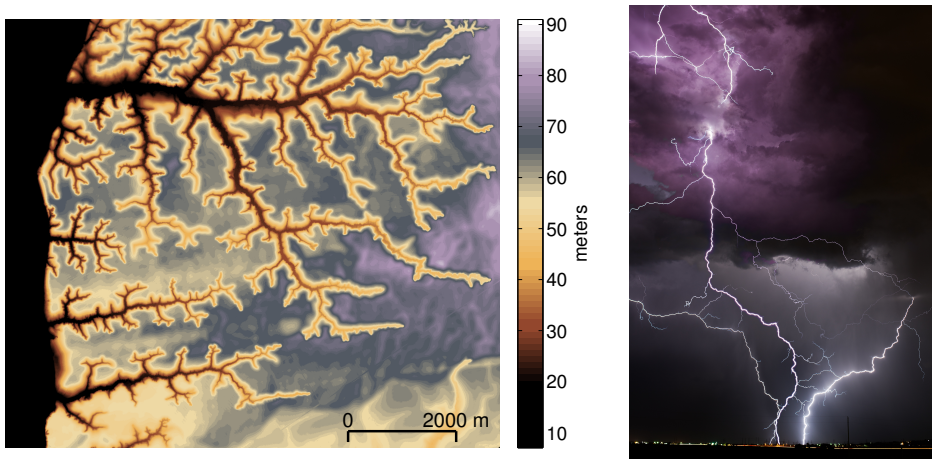

(a) (b)

Figure 1-2: Some examples of growth in a Poisson (or Laplacian) field. (a) A groundwater-fed network of streams in Bristol, Florida. (b) Lightning formed by dielectric breakdown of the air.

The bulk effect of these processes is termed *soil creep*. And the rate of soil for sufficiently shallow slopes appears to be proportional to the topographic slope (Culling, 1960, 1963), which suggests that soil creep in such a regime is not so unlike *diffusion*. This process will be more deeply discussed in Chapter 2.

These two processes, seepage and diffusion, interact in a way that allows for the formation of winding streams surrounded by smooth topographic valleys on the one hand, yet a highly branched, intricate network of streams on the other. In this dissertation, I will first exhaustively examine the former, then present results that indicate how emergent properties appear on the scale of the latter. I will now proceed to review the physics of seepage. To those with an adequate understanding of groundwater hydrology, it may be prudent to accept seepage as growth in a Poisson field and move directly to the following chapter.

1.2.2 The physics of seepage

Consider an *aquifer*, which can be considered simply a volume of sediment in which water fills and can move within its pore spaces. This subterranean water, known as *groundwater*, is recharged through rainfall and emptied through the streams resulting from its reemergence elsewhere. The saturated region occupied by groundwater is

bounded from above by the *groundwater table*. Above this is a region saturated by capillary forces, known as the *capillary fringe*, but because this is generally much smaller than height of the groundwater table above the river (at maximum, $\sim 2/3$ m for dense clays, and on the order of a centimeter for quartz sand (Bear, 1972)), the flow contribution from this region can often be neglected. Some of these features can be seen in figure 1-3.

The process of reemergence, or seepage, is a pressure-induced flow through porous media exiting at a free surface (generally the point where the topography meets open air). Darcy (1856) first phenomenologically discovered the equation of motion for flow through a porous media, termed Darcy's law:

$$q = -K\nabla\mathcal{H} \tag{1.1}$$

where q is specific groundwater flux (flux per unit area, with units of m/s), K is the hydraulic conductivity of the porous media, $\mathcal{H}$ is the hydraulic head (which, for hydrostatic pressure gradients, is equivalent to the height of the groundwater table above a reference point — generally the river; we will explicitly explain this in the following section), and ∇ is the three-dimensional gradient. This constitutive equation is a Fickian law, and can be written more generally as

$$J = -D\nabla\varphi \tag{1.2}$$

where D, the diffusivity with units of m^2/s has replaced the hydraulic conductivity K, and a more general field variable φ is used. When this law is applied to the diffusion of particles, φ represents their local concentration. When applied to heat diffusion, φ can be taken to be temperature. And as in the cases of heat and particulate diffusion, Darcy's law is a continuum equation, where continuity is a valid assumption over length scales much longer than the size of a pore space. Further discussion of this approximation and its limits can be found in Bear (1972).

Combined with incompressibility of water, $\nabla\cdot q = 0$, Darcy's law becomes Laplace's

equation:

$$\nabla^2 \mathcal{H} = 0. \tag{1.3}$$

Additional approximations can be made to reduce this problem to a field over two dimensions, as we will later show.

1.2.3 The components of a groundwater system

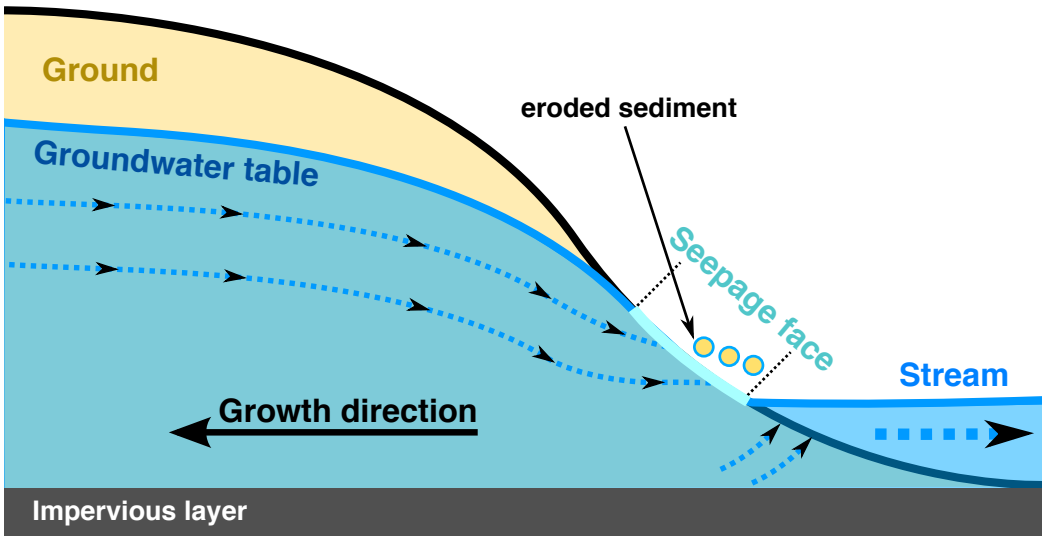

Figure 1-3: The components and flow directions of a laminar groundwater seepage system.

Let us begin by introducing and promptly discarding some common nomenclature. I framed Darcy's law in equation 1.1 in terms of the *hydraulic head*

$$\mathcal{H} = z + \frac{p}{\rho g} \tag{1.4}$$

where z is the vertical coordinate, p is gauge pressure (pressure - atmospheric pressure) of the fluid, ρ is the density of the fluid. When pressure gradients are primarily hydrostatic, this quantity is equivalent to the height of the groundwater table, and the hydraulic head is no longer dependent on z. I include this distinction here as there is a convenience in explicitly stating the dependence on z, particularly in what it intuitively reveals about the flow direction in our system as we discuss its components.

We will now briefly discuss these components, as illustrated in Figure 1-3.

The groundwater table

When *unconfined*, the aquifer is bounded above by a free surface known as the groundwater table. When flow is laminar, this surface must be a streamline in order for Darcy's law to hold while also conserving mass. In the field site in Bristol that we will subsequently analyze, the groundwater table is also bounded from below by an impervious boundary.

Stream-topography boundary

On the boundary between the stream (or more broadly, the reservoir) and the groundwater-infused sediment, $\mathcal{H}$ is constant. Such a boundary has a prescribed potential whenever a flow domain is adjacent to a body of liquid (Bear, 1972). This boundary is therefore an equipotential surface, and thus the vector $\nabla\mathcal{H}$ is perpendicular to it. Flows in such a region are therefore perpendicular to the boundary between sediment and stream, as long as both subsurface flow and stream flow are roughly laminar.

The seepage face

Finally, there exists a surface between these two regions in which water exits from the subsurface, but because of the absence of a stream of fixed height above it, it flows in a direction following the surface of the topography until it reaches the stream. This surface is called the seepage face.

The presence of such a region bridging the two streamlines is mathematically necessary to prevent the streamlines from the groundwater table and the streamlines exiting to the reservoir from intersecting. In Bristol, Florida (the field site referenced in chapters 2 and 3), their size is generally less than 1 m in headward length, and they generally appear to be saturated, muddy regions over which water flows downstream, adhering to the surface of the topography. While this definition is consistent with that which we presented above, when flux is sufficiently high, this feature often creates discrete springs.

1.2.4 The Dupuit-Forchheimer approximation, and Poisson's equation

When pressure gradients are hydrostatic, and consequently, flows are primarily horizontal, Darcy's law can be written in the Dupuit-Forchheimer approximation (Bear, 1972; Dupuit, 1863; Forchheimer, 1886):

$$q = -Kh\nabla h \tag{1.5}$$

$$= -\frac{K}{2}\nabla h^2 \tag{1.6}$$

where k is the hydraulic conductivity, h is the height of the groundwater table, and q is flux per unit length (through a vertical slice of the groundwater table). Mass conservation requires that the divergence of this flux and rainfall be reflected as a change in the height of the groundwater table, yielding the Boussinesq equation:

$$\frac{\partial h}{\partial t} = \frac{K}{2}\nabla^2 h^2 + P \tag{1.7}$$

where P is precipitation rate. However, we concern ourselves with the dynamics that occur over time scales of growth (thousands to millions of years (Abrams et al., 2009)), and we can therefore simplify this equation by considering other time scales of the problem. The time scale of relaxation of the groundwater table is $\frac{\mathcal{L}}{K} \sim 10^4$ days in Florida, where $\mathcal{L} \sim 10^2$ m is the inverse of the drainage density, and $K \sim 10^{-7}$ m/s (Petroff et al., 2013). This time scale is much greater than the time between storms (10 days), and so we treat precipitation as continuous. We can thus assume a quasi-steady state system where rainfall and flux divergence are in balance, giving us Poisson's equation:

$$\nabla^2 h^2 = -\frac{2P}{k}. \tag{1.8}$$

Or, letting $\phi = -\frac{k}{2P}h^2$,

$$\nabla^2 \phi = -1. \tag{1.9}$$

Near a channel head, we can neglect the Poisson term, giving us Laplace's equation,

$$\nabla^2\phi = 0, \tag{1.10}$$

now defined over a two-dimensional field $\phi(x, y)$ with a two-dimensional gradient.

1.2.5 Laplace's equation and conformal maps

Laplace's equation affords us the use of a number of convenient analytical tools. In particular, if we assign each (u, v) pair in the planform coordinate system to a complex number $w = u + iv$, a generalized solution to this equation is any function of the complex number w. Functions can then be chosen to satisfy the boundary conditions of a particular problem. In our case, we seek a solution around a stream defined by $v = 0$ such that $\phi = 0$ on a stream defined as the real axis. Letting $\phi = \mathrm{Im}(\Phi)$ and assuming Φ is analytic, a solution can be written as a power series expansion:

$$\Phi = a_1 w + a_2 w^2 + a_3 w^3 + \mathcal{O}(w^4)$$

satisfying the boundary condition that $\phi = 0$ when $v = 0$.

Because any analytic function $F(w)$ solves the Laplace equation, we can contort this field in almost any manner to obtain the solution around almost any boundary condition through the use of a *conformal map* $w = g(z)$.[1] Of particular interest to us is the geometry of an actively growing tip, which we can encapsulate through substitution of the conformal map

$$w = g(z) = \sqrt{z}, \tag{1.11}$$

shown in Figure 1-4. Our solution then takes the form

$$\Phi_1 = a_1 z^{1/2} + a_2 z + a_3 z^{3/2} + \mathcal{O}(z^2)$$

[1] While closed-form solutions to Poisson's equation (1.8) can be found (Cohen and Rothman, 2017), it is often not without great effort, as the boundary conditions are not conformally invariant due to the presence of the source term, $-2P/k$.

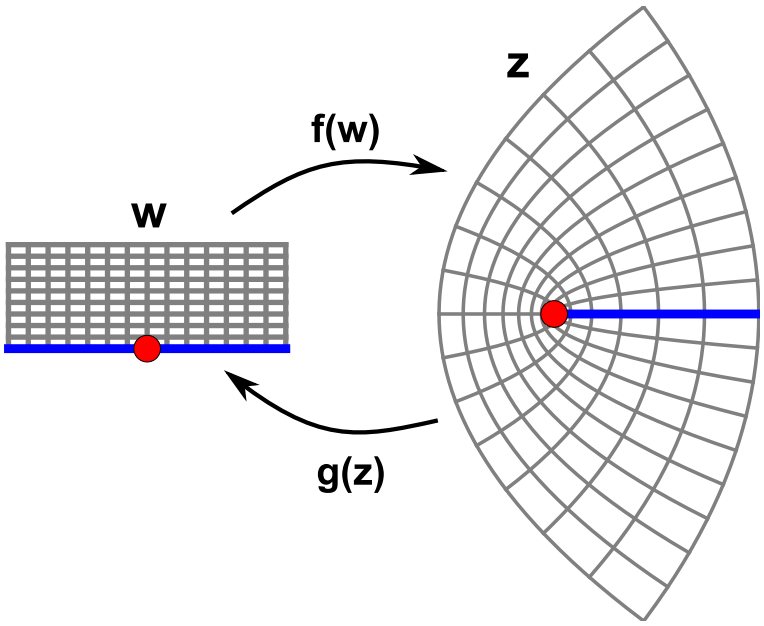

Figure 1-4: The conformal maps $f(w) = w^2$ and $g(z) = \sqrt{z}$ between the upper half plane w and a "physical" plane z that represents a stream with a spring at the origin.

where the coefficients a_i are determined by groundwater field around the tip. In particular, a_1 can be related to the flux to the actively growing channel head (Petroff et al., 2013), and recent results suggest that streams grow in a direction that minimize a_2, and equivalently, maximize the symmetry of the field around the growing tip.

1.2.6 The $2\pi/5$ branching angle

The conformal map (1.11) provides an interpretation of the water table shape around a spring, but we can choose different maps that represent almost any geometry we want, as a consequence of the Riemann mapping theorem (Weisstein, 2017b). A map of particular interest is the function

$$f(w) = w^{2c}\left(\frac{1}{c} - w^2\right)^{1-c}, \tag{1.12}$$

which maps the upper half plane to a stream confluence, as shown in Figure 1-5, where c is the angle α between the two branches as a fraction of 2π.

It can be shown that the streamlines that enter the tips generated by this map

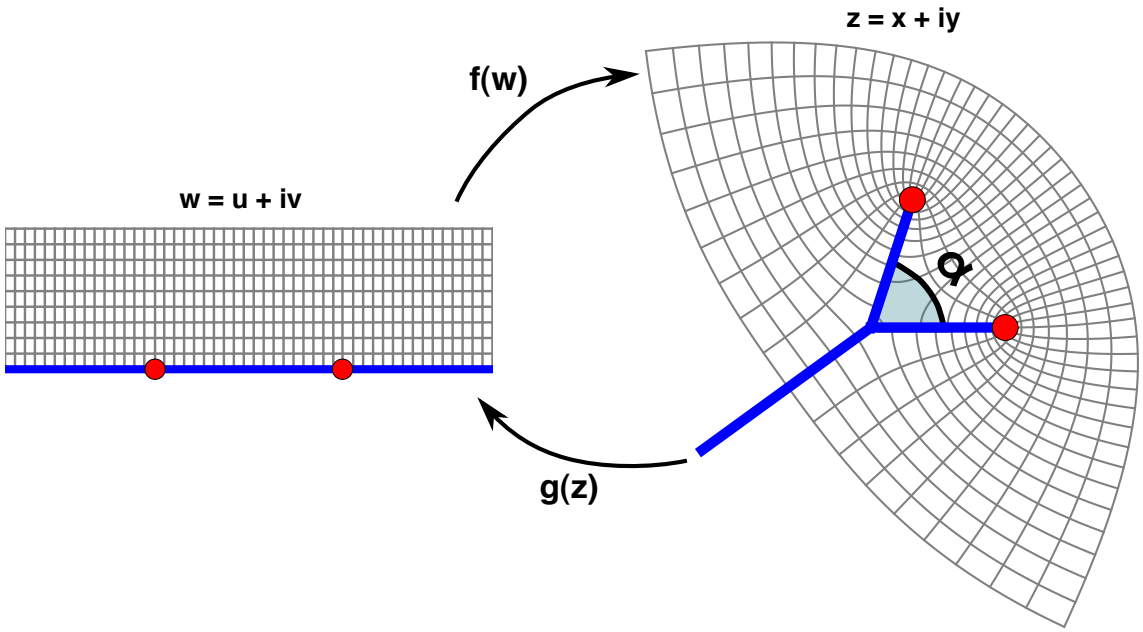

Figure 1-5: The conformal map (1.12) between the upper half plane w and the physical plane z, representing a bifurcated stream.

(defined by $w = \pm 1 + v$) enter without curving when $c = 1/5$ (corresponding to a branching angle of $\alpha = 2\pi/5$) (Devauchelle et al., 2012). Moreover, Devauchelle et al. (2012) find that the average branching angle of streams in a network of groundwater-fed streams in Bristol, Florida is $\approx 72°$, suggesting that stream networks advance in the direction of the streamline entering the tip. We mention the map (1.12) here both as an example of how the groundwater field can be contorted and because we will reference this result in Chapter 3, in which we discuss deviations from this 72° shape.

1.3 Outline

This dissertation will roughly exhibit the property that chapter number $\sim$ log scale. In Chapter 2, I will discuss how soil, over sufficiently long time scales, moves around in a manner not so unlike perfume spreading through a room or food coloring spreading through water through a process known as diffusion. I then present a simple model of valley formation by this mechanism, in which a variable diffusion coefficient gives rise

to a valley edge that fundamentally changes the shape of the valley. In Chapter 3, we will consider a network-scale phenomena: the lateral migration of streams. I will discuss how the simple interaction of reemerging groundwater and diffusing topography can give rise to produce a wide-angle confluences and network-wide fluctuations in curvature through the rearrangement of streams. Finally, in Chapter 4, I will explore rivers across the contiguous United States and present a model that suggests how branching angle can predict the aspect ratio of river basins. In particular, we find evidence that the 72° branching angle in groundwater-fed environments produces a basin aspect ratio of basin width to basin length. In addition, we explore the dependence of a relevant scaling law known as Hack's law (Hack, 1957) on climate, and find that the self-similarity of this aspect ratio breaks down for large basins.

Chapter 2

A free-boundary model of diffusive valley growth: theory and observation

Abstract

Valleys that form around a stream head often develop characteristic finger-like elevation contours. We study the processes involved in the formation of these valleys and introduce a theoretical model that indicates how shape may inform the underlying processes. We consider valley growth as the advance of a moving boundary travelling forward purely through linearly diffusive erosion, and obtain a solution for the valley shape in three dimensions. Our solution compares well to the shape of slowly growing groundwater-fed valleys found in Bristol, Florida. Our results identify a new feature in the formation of groundwater-fed valleys: a spatially variable diffusivity that can be modelled by a fixed-height moving boundary.

2.1 Introduction

Flowing water carves beautiful, diverse features into landscapes (Bierman and Montgomery, 2013). The mechanism by which it does so is fundamentally simple: water

accumulates and flows downstream, forming rivers with the capacity to transport soil and rocks and erode these landscapes (Ritter et al., 2011). Depending on the properties of the surface being eroded, different physical processes influence this erosion and consequently leave behind diverse topographic signatures. In particular, when the eroded sediment originates from the topography in the vicinity of the river, its transport downstream facilitates the formation of valleys by imposing a boundary condition to which the topography is subject. For landscapes whose surfaces are sufficiently shallow and composed of homogeneous soil rather than rock, the evolution of the surface is approximately linearly diffusive (Culling, 1960, 1963; Heimsath et al., 2005). When this sediment is transported downstream at a rate that exceeds the rate at which it is supplied, these rivers can be considered as fixed-height absorbing boundaries of diffusive topography (Petroff et al., 2012). The quasistatic topographic response to this forcing is what we call a valley, and we seek to understand the form of these valleys in what follows.

Two models describing the formation of soil-mantled valleys can be found in recent works, and both compare valley formation to other well-studied diffusive systems. Pelletier and Perron (2012) find that the parabolic isotherms predicted for a solidifying front in a temperature field (Ivantsov, 1947) agree well with the topographic contours of storm-eroded valleys in Southern Arizona, where water flows over the surface of the topography. Petroff et al. (2011) find that isolated contours of groundwater-fed valleys in Bristol, Florida are similar to the steady-state shape of the interface formed when a less viscous fluid is injected between glass plates containing a more viscous fluid (Saffman and Taylor, 1958). Both results suggest that these valleys are similar to an interface moving through a diffusive field, but because their boundary conditions differ, so too do the resulting shapes of the valley they predict.

To explore this issue, we construct a theory for valleys that diffuse around nearly stationary streams. We hypothesize that, when the streams are fed by groundwater, such valleys exhibit a height-dependent diffusivity. In an asymptotic limit, this variable diffusivity can be approximated as a fixed-height moving boundary at the rim of the valley, or *valley edge*. We introduce a free-boundary model that incorpo-

rates this element: linear diffusion of topography within an expanding valley edge of specified height. This model predicts a valley shape, which we compare both to real valleys and shapes predicted by the previously mentioned models of valley formation. This appears to be the first time that a real two-dimensional elevation field (that is, a contour map) is compared to a predicted valley shape. Our results demonstrate how physical features can be incorporated into models of valley growth as boundary conditions. By exploring this connection, we shed light on how shape can reveal the mechanisms involved in the history of valley growth.

2.2 The physical picture

We consider a model in which valleys form as surface topography diffuses into an absorbing stream. Rainsplash, vegetation growth and death, freeze-thaw cycles, and animal burrowing are the primary mechanisms that produce topographic diffusion, known as soil creep (Culling, 1963, 1965). In the continuum limit, soil creep has been observed to follow a Fickian law at shallow slopes (Culling, 1960; Dietrich et al., 2003):

$$q = -D\nabla H, \tag{2.1}$$

where H is topographic height, D is a diffusivity with units m^2/s, and q is volumetric flux per unit width. In other words, the rate at which soil travels downslope is proportional to the steepness of that slope.

2.2.1 The moving boundary

We hypothesize that the presence of groundwater renders the diffusivity D height-dependent. Because the upland region of groundwater-fed valleys is further from the water table than the sloped region within the valley, the region outside the valley is drier than within the valley. The relatively flat upland also receives more insolation, amplifying the effect. Depending on climate, vegetation may also enhance it. The relative dryness outside the valley increases the diffusivity (Herminghaus, 2005; Roer-

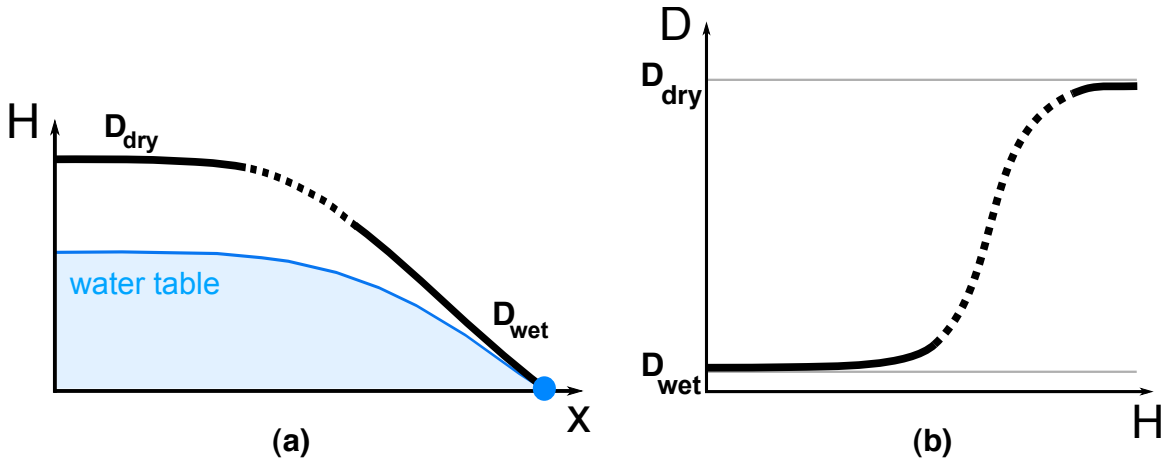

Figure 2-1: Schematic illustration of the variability of diffusivity with height H. (a) A vertical cross-section through a valley with diffusivities D_{wet} at small H and D_{dry} at large H. The transitional region is indicated by the dotted line. The location of the stream is indicated by the dot on the x axis. (b) The function $D(H)$, which we assume varies rapidly near the valley edge. The transitional region is again indicated by the dotted line.

ing, 2004; Petroff et al., 2012), producing a height-dependent diffusivity as illustrated in figure 2-1.

Taking D_{wet} to be the lower bound of the diffusivity close to the water table and D_{dry} to be the upper bound of diffusivity outside the valley, we consider the limit in which $D_{\text{wet}}/D_{\text{dry}} \to 0$. In this limit, the upland topography diffuses infinitely quickly compared to the valley, and so we take the height of the upland region to be constant. In the limit where the transitional region is thin, diffusivity is a step function at a critical height H_0. figure 2-2 shows how these approximations appear for a real valley.

This description resembles other models of moving boundaries in diffusive fields. For example, when a fluid of low viscosity slowly displaces a fluid of higher viscosity, the velocity of the two fluids must be the same on each side of the interface. The smaller viscosity of the invading fluid then requires that pressure gradients within the invading fluid be small compared to the defender. The relatively uniform pressure within the invader then translates to a constant-pressure boundary condition at the interface (Saffman and Taylor, 1958).

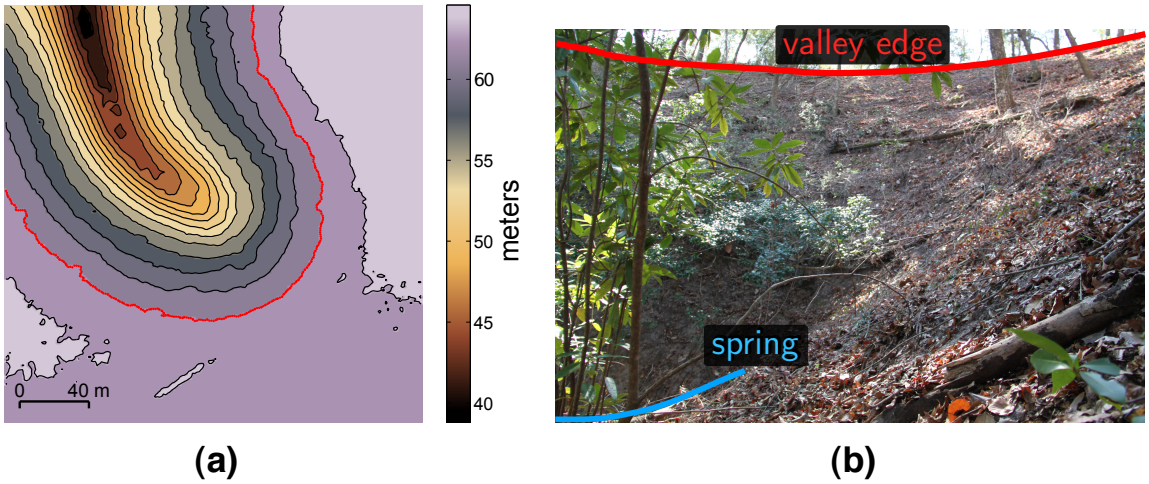

Figure 2-2: (a) A topographic map of the valley in figure 2-7a. Elevation is measured with respect to NAVD 88. The valley edge roughly corresponds to the red contour. (b) An oblique view of the interior of a real valley.

2.3 Mathematical representation

We now formalize these components into a single moving-boundary problem. By construction, our theory will model only the late stages of valley growth, where the valley edge moves much faster than the spring advances, the memory of the initial conditions has almost vanished, and we approach a characteristic shape.

Consider a valley of topographic height $H(x, y, t)$ growing around a stream γ at height $H = 0$, which flows along a path from $x = 0$ to $x \to -\infty$ along $y = 0$, as shown in figure 2-3. We write the valley edge as $\Gamma(t)$, on which $H = H_0 = \text{const.} > 0$. Let $\Omega(t)$ be the region between γ and $\Gamma(t)$. We assume that the topographic elevation, $H(x, y, t)$, is diffusive in Ω, and that the normal velocity v_n of the valley edge Γ is linearly proportional to the normal derivative of H at this edge. This velocity condition assumes that sediment flux is proportional to slope. For a very slow rate of valley growth, the time derivative in the diffusion equation can be neglected. In this quasistatic limit, our system of equations is

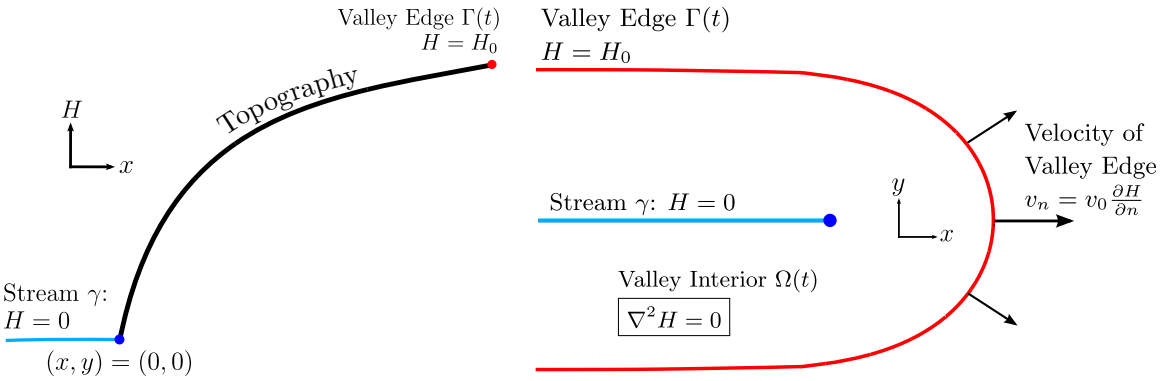

Figure 2-3: Illustration of diffusive valley growth. Left: side-view. Right: planform, top-down view.

$$\begin{aligned} H &= 0 && \text{on } \gamma \\ H &= H_0 && \text{on } \Gamma(t) \\ v_n &= v_0 \frac{\partial H}{\partial n} && \text{on } \Gamma(t) \\ \nabla^2 H &= 0 && \text{in } \Omega(t). \end{aligned} \tag{2.2}$$

We nondimensionalize distance and time, setting $h = H/H_0$, $x \to x/H_0$, $y \to y/H_0$, and $t \to v_0 t/H_0$. The system of equations becomes

$$\begin{aligned} h &= 0 && \text{on } \gamma \\ h &= 1 && \text{on } \Gamma(t) \\ v_n &= \frac{\partial h}{\partial n} && \text{on } \Gamma(t) \\ \nabla^2 h &= 0 && \text{in } \Omega(t). \end{aligned} \tag{2.3}$$

The solution to this problem satisfies a kind of shape invariance, namely

$$h(r^\alpha x, r^\alpha y, rt) = h(x, y, t), \tag{2.4}$$

which is to say that the valley grows outwards as time increases. A shape invariant solution will necessarily satisfy the initial condition $\Gamma(0) = \gamma$. In fact, we will find that $\alpha = \frac{1}{2}$ as would be expected for a diffusive process.

To see this, we consider the behaviour of h for large, negative values of x far away from the stream tip $(x, y) = (0, 0)$. From the boundary conditions, we expect that any oscillations or perturbations in Γ to be damped out with time. Because γ is stationary, h should become independent of x for large, negative x, so $\frac{\partial h}{\partial x} = 0$. Then, because $\nabla^2 h = 0$ in Ω, we have $\frac{\partial^2 h}{\partial y^2} = 0$, so h is a linear function of y from $y = 0$ to the boundary $y = L(t)$, where L is the limiting half-width of Ω as $x \to -\infty$. This has the linear solution $h(x, y, t) = |y| / L$. From the boundary condition we have $\frac{dL}{dt} = v_n = \left|\frac{\partial h}{\partial y}\right| = \frac{1}{L}$ on the boundary $y = \pm L$, giving $L = \sqrt{2t}$.

Now that we know the shape of Ω in the limit as $x \to -\infty$, we solve for the full shape. We conformally map Ω to the upper-half plane, which is possible by the Riemann mapping theorem. This allows us to solve Laplace's equation $\nabla^2 h = 0$ in the upper-half plane and then transform it back to our original coordinate system, as Laplace's equation remains unchanged by conformal maps. At this point it becomes useful to use complex coordinates $z = x + iy$ to describe Ω and h. We seek a map from z to $\zeta = \xi + i\eta$ which sends Ω to the upper-half plane $\eta > 0$, Γ to the interval $\eta = 0, -1 < \xi < 1$, and γ to the two intervals $\eta = 0, |\xi| > 1$. The upper edge of γ goes to $\xi > 1$ and the lower edge goes to $\xi < 1$. An illustration of this map is shown in figure 2-4. The required map is found in Appendix 2.A and is given by

$$\frac{z}{\sqrt{2t}} = \frac{2}{\pi} + \frac{\zeta}{\pi} \log\left(\frac{\zeta - 1}{\zeta + 1}\right). \tag{2.5}$$

Now working in the ζ-plane, we can find $h(\zeta)$ as a solution to Laplace's equation $\nabla^2 h = 0$ in the region $\eta > 0$ with the boundary conditions that $h = 1$ on the interval $\eta = 0, -1 < \xi < 1$ and $h = 0$ on the two intervals $\eta = 0, |\xi| > 1$. Particularly since h is a function of ζ alone and does not vary in time in the ζ-plane, this forces h to satisfy the shape invariance discussed above. We write h as the imaginary part of a function $\omega = \phi + ih$, which is analytic on the upper-half plane. The relation

$$\omega = \frac{1}{\pi} \log\left(\frac{\zeta - 1}{\zeta + 1}\right) \tag{2.6}$$

satisfies these conditions.

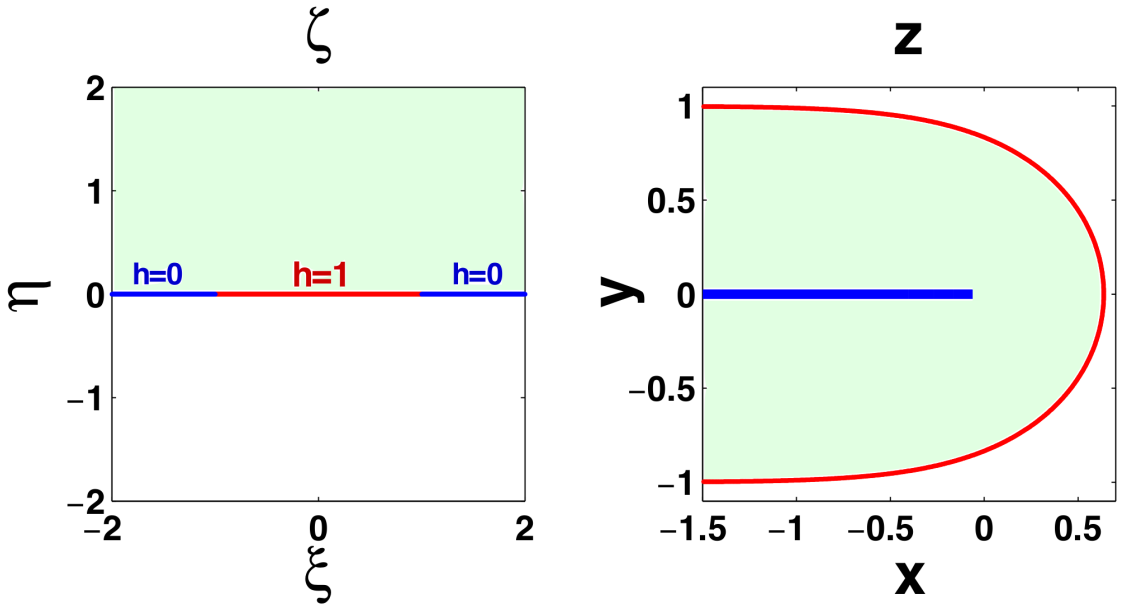

Figure 2-4: An illustration of the conformal map from the physical coordinates $z = x + iy$ to the mathematical coordinates $\zeta = \xi + i\eta$. The blue line in both plots indicates the stream γ, the red line indicates the valley edge Γ, and the light green region indicates the domain Ω.

Combining equations (2.5) and (2.6) we can relate z to ω through

$$\frac{z}{\sqrt{2t}} = \frac{2}{\pi} - \omega \coth \frac{\pi\omega}{2}. \tag{2.7}$$

Taking the imaginary part of ω as a function of z lets us recover the height h as a function of x and y. In particular, restricting to $h = 1$ yields a relationship between x and y on the boundary $\Gamma(t)$:

$$x = \frac{2}{\pi}\sqrt{2t} + \frac{y}{\pi} \log\left(\frac{\sqrt{2t} - y}{\sqrt{2t} + y}\right). \tag{2.8}$$

A 3D perspective view of the full solution is shown in figure 2-5. For convenience, we henceforth refer to our model as the *Fickian finger* model, so named for the linear dependence of soil creep on slope reminiscent of Fick's first law of diffusion and the finger-like shape of the valley edge.

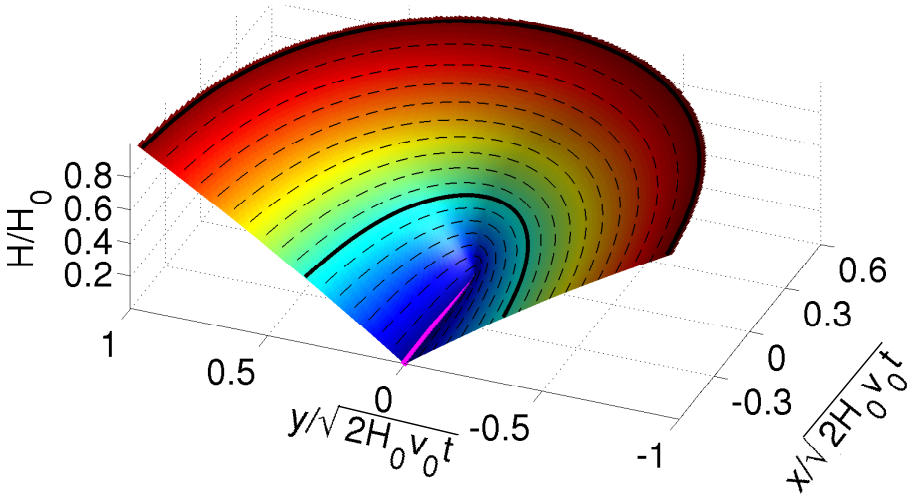

Figure 2-5: Solution to equation (2.2). The straight magenta line indicates the location of the stream. The bold contour is at $H_0/3$.

2.4 Selection of slow-growing valleys

To test our mathematical formulation, we compare the Fickian finger model to valleys within a network of groundwater-fed streams in Bristol, Florida. Valleys in this area are composed primarily of homogeneous, unconsolidated quartz sand (Schumm et al., 1995; Abrams et al., 2009).

Our model focuses on a slow-growing regime where diffusive relaxation is linear and the stream head does not advance. Consequently, selected valleys must have shallow slopes to be slow-growing and maintain linear transport. Moreover, they should be isolated from other valleys to reduce the influence of non-local effects. Practically, we seek two properties associated with these criteria: we seek to minimize the proportion of each valley with slopes steeper than the angle of repose, and we seek to maximize distance to the nearest downstream branch.

To find fraction of the valley area that is at or above the critical slope, we use a flow accumulation model (Tarboton, 1997) to determine contributing topographic areas to each stream head, then find regions whose slopes are greater than 0.5, or 26.6°. This is a loose threshold for the angle of repose, which is generally higher than 30° for dry grains (Nowak et al., 2005). We determine the length of channels by calculating the arclength along extracted streams from stream tips to the nearest

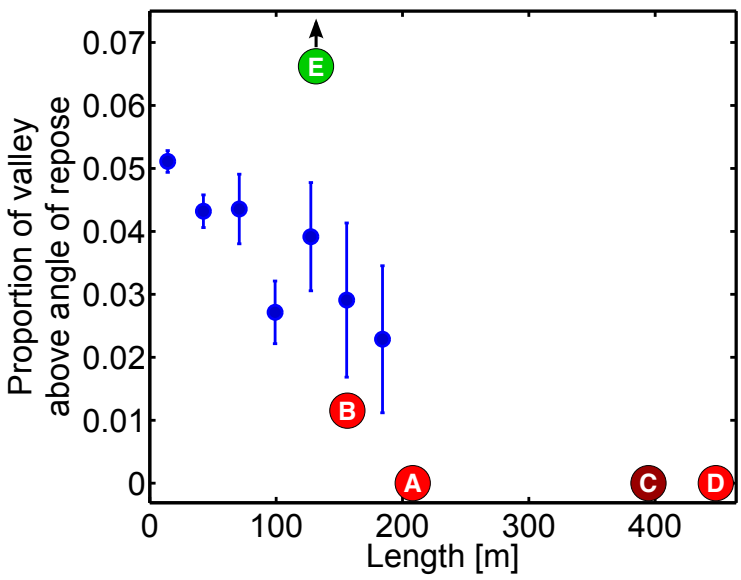

Figure 2-6: The fraction of the valley (extracted by the flow accumulation algorithm of Tarboton (1997)) that is above the angle of repose as a function of channel length. The fitted valleys in figure 2-7, shown here in red, fall at the end of this trend – long and largely below the threshold of motion. Valley E (green) is a poorly-fitting head, shown in figure 2-9. The arrow above valley E indicates that the actual proportion of valley E above the angle of repose is 0.17. See Appendix 2.B for further discussion.

downstream junction. We find a linear trend with the proportion of area above the angle of repose, shown in figure 2-6. This suggests that valleys with longer streams are diffusively dominated, and we find several valleys which fall at the end of this trend, indicated by red circles in figure 2-6. These valleys can be characterized as long, unbranched, and gently sloped.

2.5 Comparison to field data

We now proceed to compare valleys A-E in figure 2-6 to our model. For each valley, topographic relief was obtained through laser altimetry data with a horizontal resolution of 1.2 m and a vertical resolution of about 5 cm (Devauchelle et al., 2012). The valley was then rotated in the horizontal plane such that the first twenty meters of stream from the stream head were aligned with the stream of the theoretical valley. We then fit 5 parameters (three coordinates for the position of the channel head, one scale factor for topographic height, and one scale factor for valley width and length)

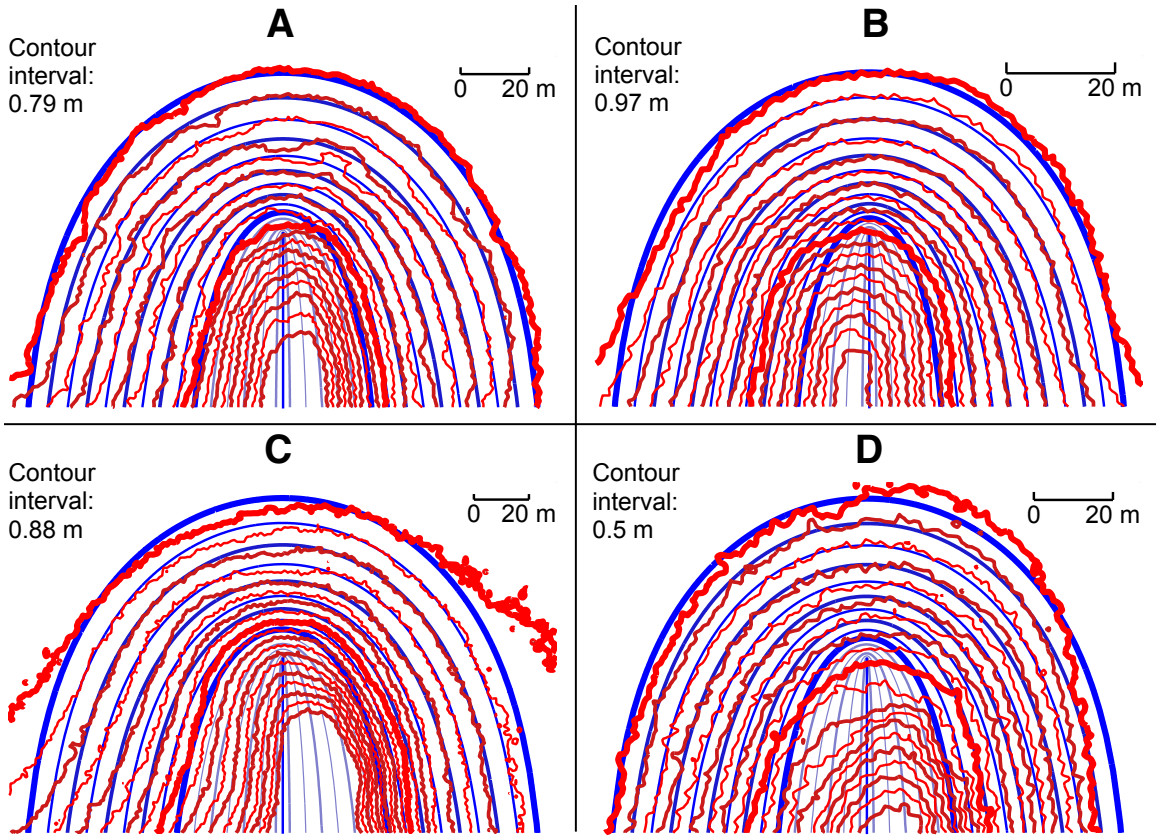

Figure 2-7: Fits of our model to several slow-growing valleys. The bold interior contour is at $H_0/3$. The outermost contour shown in A is the red contour indicated in figure 2-2.

to minimize the least-squares difference between the elevations of the two surfaces.

We find that the upper two-thirds of valleys specified in figure 2-6 agree well with our theoretical shape, shown in figure 2-7. This agreement suggests that large regions of these valleys behave diffusively within the boundaries of the constant-height valley edge predicted by the theory. Appendix 2.B presents the contexts of these valleys within the network.

These valleys fit poorly within the bottom third of the valley (the region inside the bold contour in figures 2-5 and 2-7). We attribute the poor fit in this region to an inability of the topography to sustain the infinite slope at the stream head associated with the $h \sim \sqrt{x}$ headward profile (see Appendix 2.C). Figure 2-8 exposes this problem. An alternative boundary condition could be an interior absorbing contour that surrounds the singular river and represents the valley floodplain (a region that is

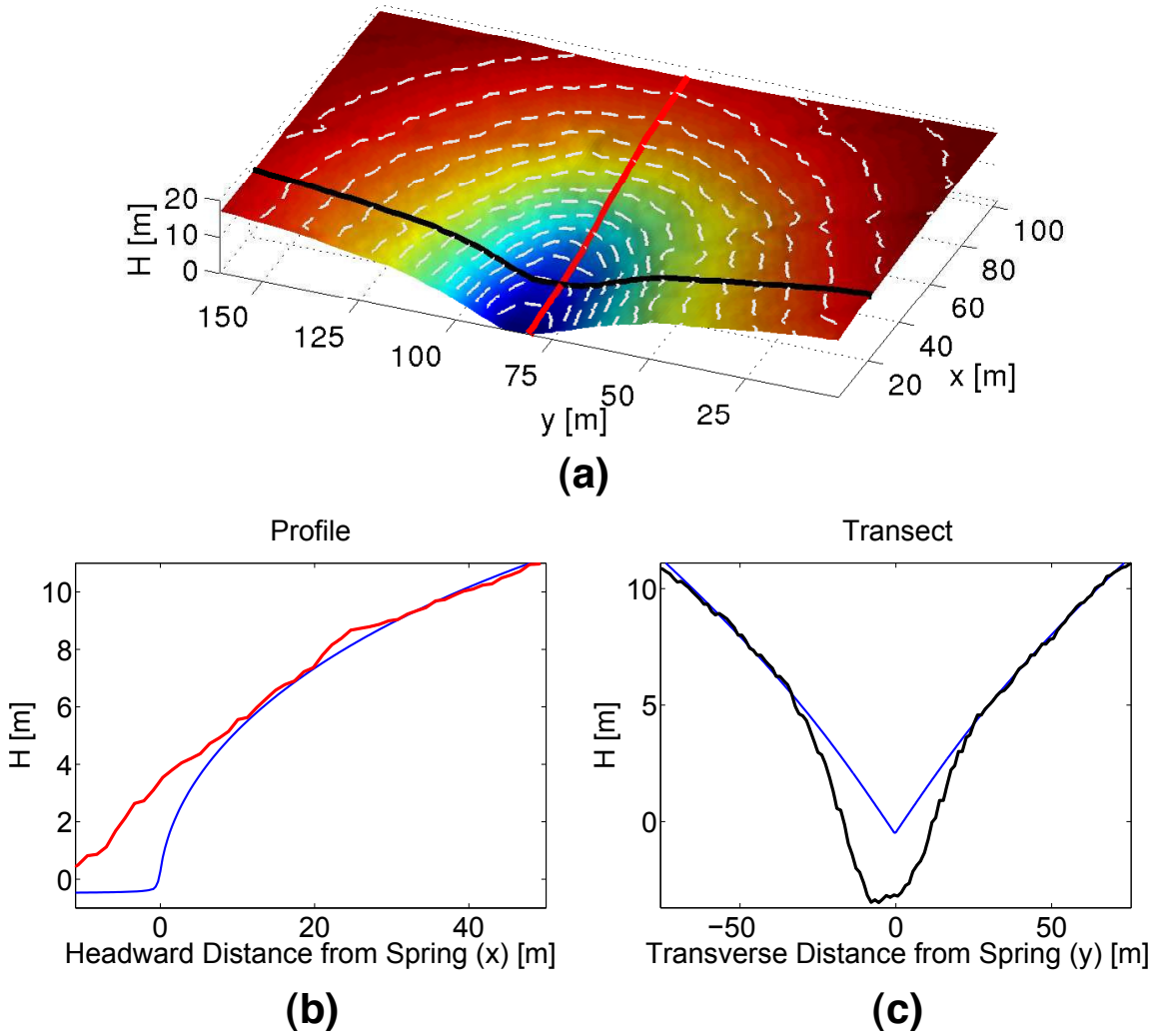

Figure 2-8: (a) A perspective plot of the valley in figure 2-7a. The headward valley relief (b) and the valley relief perpendicular to the direction of growth 30 meters downstream from the extracted spring (c) for the valley in figure 2-7a are shown in red and black, respectively. The theoretical profile and transect are shown in blue. The misfit near the stream reflects the inability of landscapes to sustain the infinite slope of the $H \sim \sqrt{x}$ profile predicted by our theory.

flooded during storms, and thus may intermittently act as an absorbing boundary), as proposed by Pelletier and Perron (2012). If we constrain an interior contour of our solution such that its growth scales with the size of the valley and stays at a height $h = 0$, we find, however, that our problem becomes overspecified. The solution to this free boundary problem is the same as that which we solved earlier, and the shape of the interior boundary is a chosen contour of our present solution. The solution around an infinitely thin needle-shaped boundary, therefore, fully represents our class

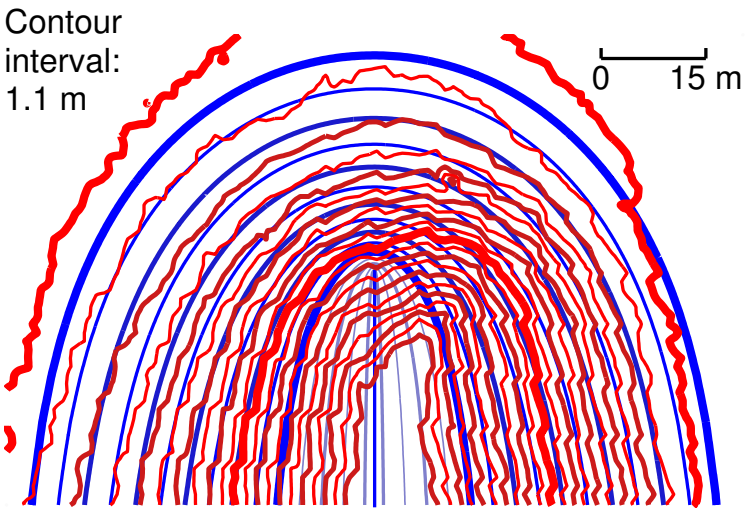

Figure 2-9: An example of a poorly fitting valley (valley 'E' in figure 2-6). Contour lines of the topographic relief are fit to and superimposed over contours of the Fickian finger model. Appendix 2.B presents the context of this valley within the network.

of solutions. However, solutions around a contour that does not scale linearly with the size of the valley may produce different results.

We also compare our solution to a valley with higher sediment flux (marked in green in figure 2-6), as shown in figure 2-9. We find that it fits poorly by comparison, supporting our premise that the Fickian finger model best approximates end-member, slow-moving valleys.

2.6 Comparison to other models

2.6.1 Ivantsov parabolic front (Pelletier and Perron, 2012)

Pelletier and Perron (2012) give the only previous theoretical model for a valley growing in three dimensions, using the solution of Ivantsov (1947) for the temperature field around a crystalline needle. Their model solves a steady-state diffusion equation

in a moving reference frame:

$$\begin{aligned} H &= 0 && \text{in } \gamma_p \\ H &= H_\infty && \text{as } x \to \infty \text{ and } y \to \pm\infty \\ -v_s \frac{dH}{dy} &= \kappa \nabla^2 H \end{aligned} \tag{2.9}$$

where γ_p indicates the valley floor, or floodplain, bounded by a parabola $x \sim -y^2$, H_∞ is the asymptotic height of the topography in the upland, κ is a diffusivity, and v_s is the velocity of the stream tip.

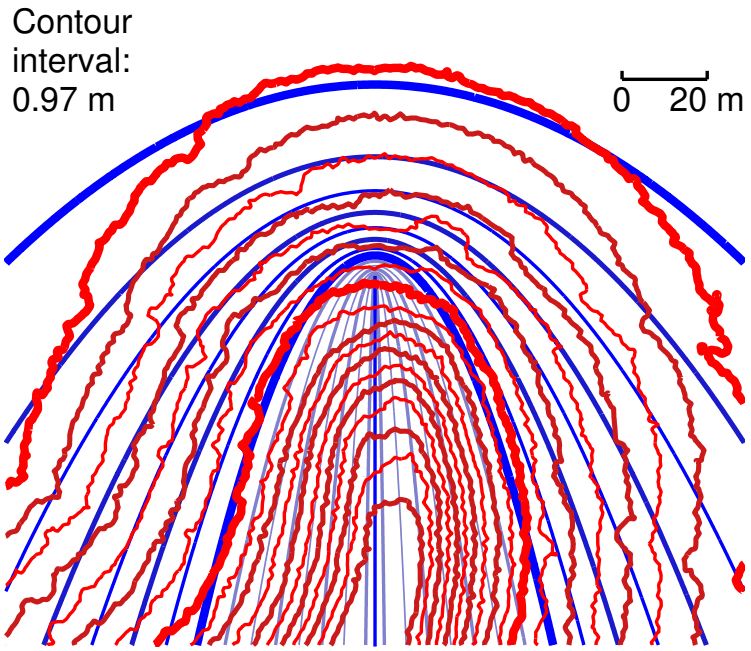

Figure 2-10: The valley of figure 2-7(a) fit to the Pelletier and Perron (2012) model.

Figure 2-10 shows that this model fits poorly to the valley head in figure 2-7(a). This misfit results from physical differences between the models: the Pelletier and Perron (2012) solution describes a steady-state form as diffusion balances the advance of the stream head, while the Fickian finger model describes relaxation around a stationary stream.

A distinguishing feature of the Pelletier-Perron model is that the contours are unbounded in y as $x \to -\infty$, which result from the advance of the stream head.

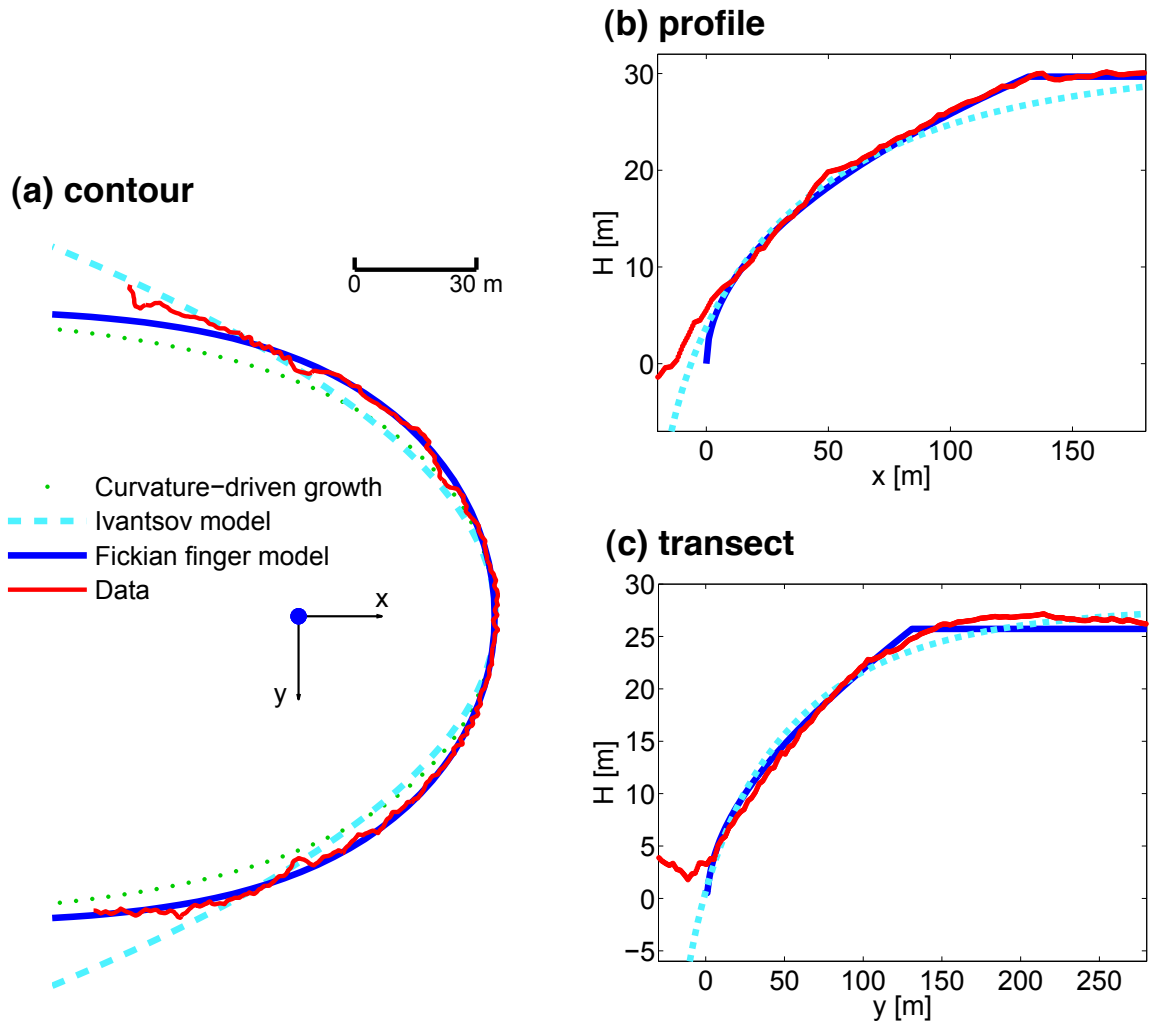

Figure 2-11: A shape comparison for three different valley shape theories. Features of the Fickian finger model are shown in blue, the log-cos contour of Petroff et al. (2011) is shown in dotted green, features of the Ivantsov solution are shown in dashed cyan, and data from the valley in figure 2-7(a) is shown in red. The blue dot in (a) indicates the location of $(0, 0)$ in the Fickian finger model.

In their model, the topography downstream of an advancing stream head has had a longer time to diffuse than topography in the vicinity of the stream head, so the valley grows wider downstream. On the other hand, bounded contours would indicate that the stream head is moving forward at a negligible velocity. The absence or presence of bounded contours can therefore reveal whether or not the stream head is advancing.

2.6.2 Curvature-driven growth (Petroff et al., 2011)

The shape of the valley edge predicted by our theory bears remarkable similarity to the contour shape predicted by Petroff et al. (2011). Our theory predicts the shape

$$x = \frac{2l}{\pi} + \frac{y}{\pi} \log\left(\frac{l-y}{l+y}\right), \tag{2.10}$$

which originates from the conformal map in equation (2.5). Petroff et al. (2011) predict a contour of the form

$$x = \frac{2l}{\pi} + \frac{2l}{\pi} \log\cos\left(\frac{\pi y}{2l}\right), \tag{2.11}$$

identical to the Saffman-Taylor finger (Saffman and Taylor, 1958), which Petroff et al. (2011) obtain from an assumption of curvature-driven growth. A notable difference between (2.10) and (2.11) is the aspect ratio set by the product $2l\kappa$, where κ is the curvature of the contour at $y = 0$ and l is the asymptotic half-width of the contour as $x \to -\infty$. For the Fickian finger valley edge, this product is $8/\pi \approx 2.55$, while for the contour of Petroff et al. (2011), this product is π (Petroff et al., 2011). A comparison between the contours predicted by the two theories is shown in figure 2-11(a).

Aside from the fact that the Fickian finger model incorporates a third dimension (the height of the diffusive field) that the Petroff et al. (2011) model does not, the shape difference can be attributed to the different growth laws on the moving boundary. The valley edge of the Fickian finger grows at a velocity $v_n = v_0 \frac{dH}{dn}$, while the model of Petroff et al. (2011) grows at a rate proportional to the local curvature.

2.7 Conclusion

We have tested the hypothesis that topographic relaxation can be described simply as linear diffusion of topographic height within a constant-height, expanding boundary. We find agreement of real valleys to the shape predicted by this theory, providing us with strong, novel evidence for both linear diffusion as a responsible mechanism and

an elevation-dependent diffusivity in groundwater-fed valleys. In particular, our results reveal a separation of timescales between the wet valley and the dry upland that produces an interface along which we can prescribe a constant height and diffusive rate of growth. Moreover, through comparison of the Fickian finger model to other models of valley growth, we deduce that bounded, "finger-like" contours suggest that the stream head within a valley is either not advancing or advancing slowly. Our results suggest that the shape of a valley can inform our understanding of the physical processes that generate these shapes. Further study of other end-member valleys may yet reveal other properties that impart their own unique topographic signatures on the geometry of valley growth.

2.A The conformal map

The map $z = f(\zeta)$ from the upper half of the ζ-plane to Ω is such that $\Gamma(t)$ maps to $\eta = 0$, $|\xi| < 1$, and γ to $\eta = 0$, $|\xi| > 1$, where the rays $\xi > 1$ and $\xi < -1$ map to the upper and lower edges of the stream, γ, respectively. The points $\zeta = \pm 1$ map to $z = \infty$ and the 'strip'-like structure of width $\sqrt{8t}$ as $z \to \infty$ suggests that the map has the form

$$\frac{z}{\sqrt{2t}} = C + \frac{g(\zeta)}{\pi} \log\left(\frac{\zeta - 1}{\zeta + 1}\right), \tag{2.12}$$

where $g(\zeta)$ is some analytic function of ζ, which will be found below, and C is a constant. The valley symmetry and the oddness of the logarithm in (2.12) with respect to ζ demands that $g(\zeta)$ be an odd function of ζ and so $g(\zeta) = \cdots + b_3\zeta^{-3} + b_1\zeta^{-1} + a_1\zeta + a_3\zeta^3 + \cdots$, where a_i and b_i are constants. Since the point $\zeta = 0$ maps to a finite point on $\Gamma(t)$, it follows that $b_i = 0\ \forall i$. Further, requiring that the map be univalent implies $a_i = 0\ \forall i \geq 3$. Since $\Im(z/\sqrt{2t}) \to \pm 1$ as $z \to \infty$ or, equivalently, $\zeta \to \pm 1$ it follows $a_1 = 1$. Thus, $g(\zeta) = \zeta$, so the map (2.12) takes the form

$$\frac{z}{\sqrt{2t}} = C + \frac{\zeta}{\pi} \log\left(\frac{\zeta - 1}{\zeta + 1}\right), \tag{2.13}$$

and it remains to determine C which is clearly real by symmetry. Now $\zeta \to \infty$ maps to the point $z = 0$ and locally the map must behave like $z \sim \zeta^{-2}$ in this limit. Expanding (2.13) for large ζ gives $C = 2/\pi$ and, finally, the map (2.5).

2.B Context of valleys in figures 2-7 and 2-9

In figure 2-12, we show the contexts of valley heads from figure 2-7 and figure 2-9 within the network. The tendency of the heads from figure 2-7 to be long and have at most small regions that are above threshold of motion suggests that these indeed represent diffusive, end-member valleys. The valley from figure 2-9 is shorter with a greater proportion of area above the angle of repose, which suggests that this valley is growing faster.

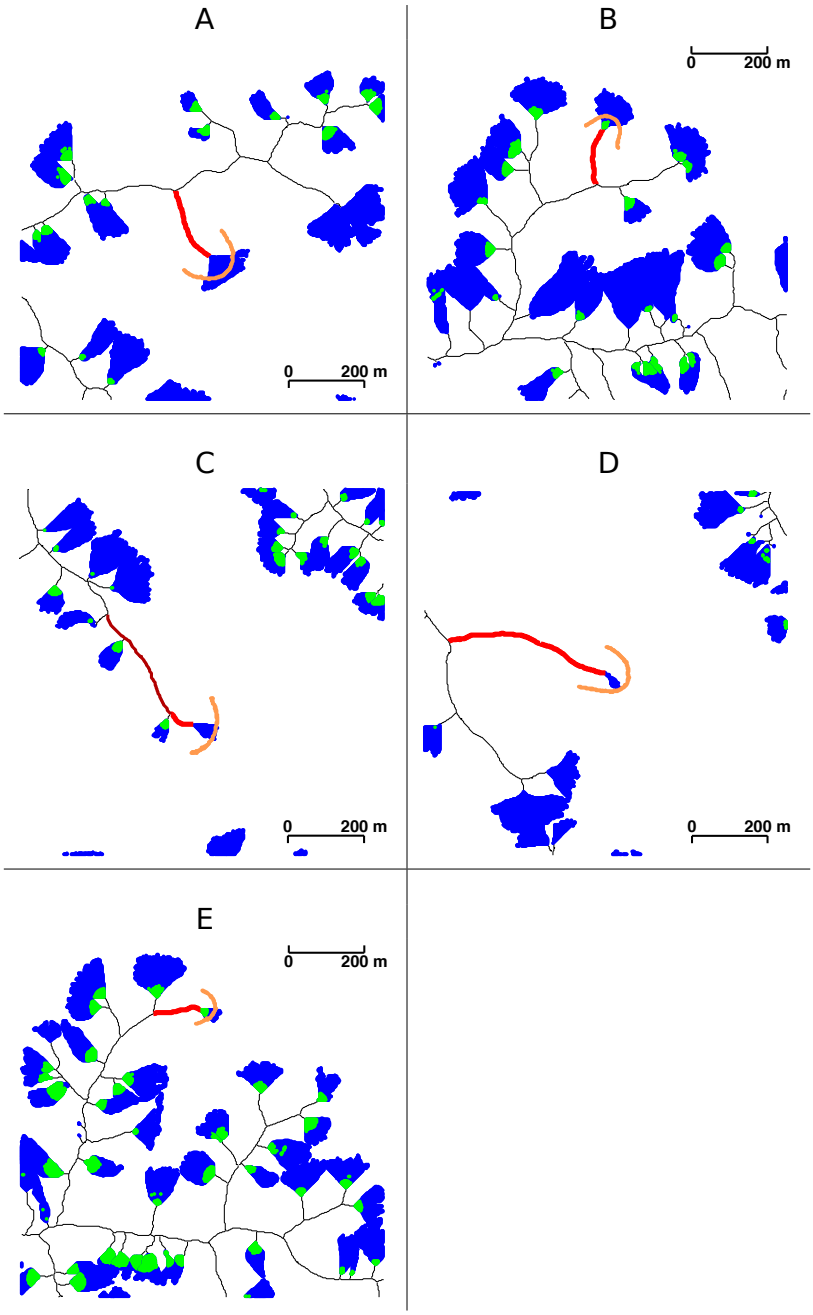

Figure 2-12: The locations within the network for the valleys shown in figure 2-7. As in figure 2-7, the contributing area is shown in blue calculated through a flow accumulation model (Tarboton, 1997), and regions above the angle of repose are shown in green. The first-order channel is indicated in red. The second-order channel for valley C is coloured a darker red to suggest that this channel may also be considered long and isolated. The orange contours indicate the location of the outermost contour of the fits in figure 2-7.

2.C Mathematical remarks

At the head of the valley ($y = 0$), the valley height $h(x, t)$ is given by

$$\frac{\pi x}{\sqrt{8t}} = 1 - \frac{\pi h}{2} \cot\left(\frac{\pi h}{2}\right), \tag{2.14}$$

for $0 < x/\sqrt{2t} < 2/\pi$. Since $2/\pi < 1$ the valley is steeper at its front compared to far downstream, and for $x \ll \sqrt{2t}$, (2.14) gives the local shape of the valley as $h \sim x^{1/2}$.

The free boundary problem (2.3) is, after suitable transformation, mathematically equivalent to that considered by Howison (1988) and Howison and King (1989) for the coating of a semi-infinite plate by a viscous fluid. To see this, consider the Baiocchi transformation (Cummings et al., 1999): define the real function Ψ, the Schwarz potential, by

$$\Psi = \frac{z\bar{z}}{4} - \frac{1}{4}\int^z g dz - \frac{1}{4}\overline{\int^z g dz}, \tag{2.15}$$

where $g(z, t)$ is the Schwarz function of the boundary of Ω, i.e. $g(z, t) = \bar{z}$ on it. Note that (2.15) gives $\nabla^2\Psi = 1$ in Ω and $\Psi_z = \Psi_{\bar{z}} = 0$ on the boundary, which, in turn, implies $\Psi = \partial\Psi/\partial n = 0$ on it. Also, $\dot{\Psi} = -p(x, y)$ (see e.g. Cummings et al. (1999)) where $p = h(x, y) - 1$, and it follows that Ψ satisfies the free boundary problem

$$\begin{gathered} \nabla^2\Psi = 1, \quad \text{in} \quad \Omega(t), \\ \Psi = 0 \quad \text{and} \quad \partial\Psi/\partial n = 0 \quad \text{on} \quad \Gamma, \\ \Psi = t \quad \text{on} \quad \gamma. \end{gathered} \tag{2.16}$$

Howison (Howison, 1988) uses potential plane methods to derive the map (2.5) to solve (2.16) and obtain the free boundary shape (2.8). Howison & King (Howison and King, 1989) later used the alternative method of Polubarinova-Kochina (Polubarinova-Kochina, 1962) to solve (2.16).

Chapter 3

Symmetric rearrangement of groundwater-fed streams

Abstract

Streams shape landscapes through headward growth and lateral migration. When these streams are primarily fed by groundwater, recent work suggests that their tips advance to maximize the symmetry of the local Laplacian field associated with groundwater flow. We explore the extent to which such forcing is responsible for the lateral migration of streams by studying two features of groundwater-fed streams in Bristol, Florida: their confluence angle near junctions and their curvature. First, we find that, while streams asymptotically form a 72° angle near their tips, they simultaneously exhibit a wide 120° confluence angle within $\sim$ 10 m of their junctions. We show that this wide angle maximizes the symmetry of the groundwater field near the junction. Second, we argue that streams migrate laterally within valleys and present a new spectral analysis method to relate planform curvature to the surrounding groundwater field. Our results suggest that streams migrate laterally in response to fluxes from the surrounding groundwater table, providing evidence of a new mechanism that complements Laplacian growth at tips.

3.1 Introduction

River networks form captivating geometries, but their present-day position often obscures the rich history of their growth and evolution (Ritter et al., 2011). Fortunately, the processes that shape this history, such as the migration of river bends (Hickin and Nanson, 1984; Bierman and Montgomery, 2013), stream capture (Howard, 1971b; Willett et al., 2014), and confluence movement and development (Carey et al., 2006; Unde and Dhakal, 2009), often leave behind morphological evidence. However, such processes have not been well-studied for groundwater-fed streams. In such landscapes, reemerging groundwater erodes surface grains by sapping and undermining hillslopes (Dunne, 1990; Howard and McLane, 1988), forming shallow streams and steep ravines around them. These streams advance in a planimetric direction that has been shown to be largely determined by the shape of the surrounding groundwater field rather than dynamics within the stream (Cohen et al., 2015; Devauchelle et al., 2012; Petroff et al., 2013). For a confluence, this appears as an angle of 72° between confluent streams, and these observations have been observed in the planimetry of a groundwater-fed channel network in Bristol, Florida (Devauchelle et al., 2012).

However, there is no indication that the current position of channels within valleys in such networks represents the history of their growth. We therefore consider a third phase of growth: lateral stream rearrangement. We suggest that this rearrangement is also influenced by the surrounding groundwater field. In particular, we hypothesize that lateral migration is driven by variable flux to either side of a stream and the subsequent filling-in of old stream paths through soil creep. Here we study two morphological features of a groundwater-fed river network to constrain the extent to which this groundwater field can describe network-wide morphology: confluences and planform curvature.

This rearrangement may be of global interest. Recent work has demonstrated that an average branching angle of 72° appears in humid climates (Seybold et al., 2017), suggesting that the influence of groundwater on global river planform morphology may be widespread wherever shallow groundwater is present. Understand-

ing and quantifying stream morphology as influenced by groundwater reemergence may therefore be of heightened importance for those interested in both scientific and application-driven pursuits that are influenced by stream migration: for example, the interactions between river migration and riparian vegetation (Perucca et al., 2006), river restoration (Palmer et al., 2005), etc.

In what follows, we present evidence of this rearrangement from a network of streams in Bristol, Florida and discuss how it may arise. We first review a theoretical framework that gives the shape of the groundwater table and the 72° branching angle. We then present an averaging scheme that reveals a striking wide-angle deviation from the predicted branching angle of 72° near the junctions of first-order confluences in Bristol, Florida. We then present a model for the migration in response to asymmetry in the groundwater field that predicts the observed deviation. Finally, we find evidence for network-wide river migration and find a length scale of curvature fluctuation that agrees with the length scale of the confluence deviation, suggesting that forcing from groundwater may influence stream planimetry throughout the network.

3.2 Background

3.2.1 Groundwater flow

Groundwater-fed channels advance as reemerging groundwater erodes material, causing the intersection point between the groundwater table and the ground to retreat, thereby extending the channel (Dunne, 1990). We begin by introducing a theoretical framework that can describe these dynamics. Consider a lone channel advancing in a groundwater field. Pressure gradients from the surrounding groundwater table determine where and how the groundwater flows into this channel (Darcy, 1856; Polubarinova-Kochina, 1962). When these gradients are hydrostatic and flows are approximately horizontal, groundwater flux q (per unit length in the horizontal plane) can be be simply described through Darcy's law in the Dupuit approximation (Darcy,

1856; Dupuit, 1863; Bear, 1972):

$$q = -kh\nabla h \tag{3.1}$$

where k is hydraulic conductivity, and h is the height of the groundwater table. Mass conservation between flux out of the groundwater table and precipitation into it yields Poisson's equation for h^2 (Bear, 1972):

$$\nabla^2 h^2 = -\frac{2P}{k} \tag{3.2}$$

where P is the precipitation rate. Sufficiently close to a stream, precipitation P can be neglected, yielding Laplace's equation (Devauchelle et al., 2012; Petroff et al., 2013):

$$\nabla^2 h^2 = 0 \tag{3.3}$$

This equation can be solved around a real channel network, and this solution has been shown to accurately predict the shape of the water table (Abrams et al., 2009) and flow into the channel network (Petroff et al., 2011).

3.2.2 Growth direction

The solution to (3.3) can be combined with a growth hypothesis to predict how the channels grow forward. Recent results suggest that streams grow in a direction that can be equivalently described by three growth hypotheses: streams maintain symmetry of the groundwater table around the spring as they grow, streams grow in the direction of the streamline entering the spring, and streams grow in the direction of maximum flux entering the tip (Cohen et al., 2015; Devauchelle et al., 2017). When a channel develops a confluence upstream, the streamlines enter the springs without curving when the angle between the confluent streams is 72° (Devauchelle et al., 2012; Petroff et al., 2013). If streams advance at an angle narrower than 72°, the streamlines entering the two springs will bend away from each other; if streams advance at an angle wider than 72°, the streamlines entering the springs will bend toward each

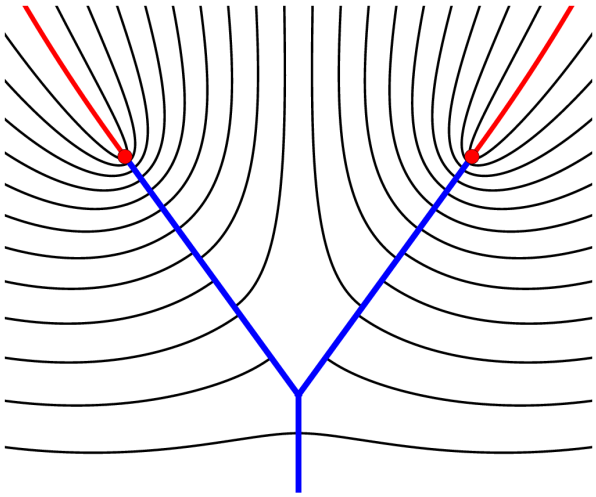

Figure 3-1: Streamlines around a confluence with an angle of $2\pi/5$ between confluent streams. The tip locations are marked as red dots. The streamlines entering the tips are indicated in red, while all other streamlines are black. The stream is blue.

other (Devauchelle et al., 2012; Petroff et al., 2013). The 72° confluence therefore can be considered a stable fixed point for stream advance (Devauchelle et al., 2017). An illustration of such a confluence and its streamlines are shown in Figure 3-1.

This predicted shape agrees with the average angle at which confluent streams join in a river network in Bristol, Florida, determined by fitting individual streams to straight lines (Devauchelle et al., 2012). However, as we will demonstrate, real confluences deviate from this theory. We now proceed to briefly describe the field site used and methods employed to this end.

3.3 Confluence migration

3.3.1 Wide angle confluences in Bristol, Florida

Confluences are ubiquitous in river networks, but the often sedimentologically complex dynamics that form them thwart attempts to construct a unifying theory for their development. River confluence geometry can be influenced by a number of parameters: relative flow magnitudes and the depth of the deepest point along a stream bed (thalweg incision) (Kennedy, 1984), the overall power exerted by the net-

Figure 3-2: A confluence in the Apalachicola river network in Bristol, Florida. The white lines indicate the location of the streams with arrows denoting the flow direction.

work (Howard, 1971a), fluid and sediment transport dynamics (Best, 1988), scour depth (Mosley, 1976), among others. However, these factors may not be the primary factors influencing migration in landscapes formed primarily through erosion by groundwater reemergence.

We study streams from a network of groundwater-fed streams located on the Florida panhandle. These rivers are overlain by homogeneous sediment comprised primarily of unconsolidated quartz sand (Abrams et al., 2009) which rests atop a layer of impermeable Pensacola clay (Schumm et al., 1995). The high hydraulic conductivity $k \sim 10^{-4}$ m s^{-1} of such clean, unconsolidated sand causes rainfall $P \sim 5 \times 10^{-8}$ m s^{-1} to be quickly absorbed, prohibiting surface runoff (Abrams et al., 2009). This supports a persistent water table in the subsurface. We consider only first-order streams (those without any upstream confluences). These streams are shallow, with little evidence of scouring or deposition, negligible difference in bed height (bed discordance), minimal difference in discharge, and negligible suspended load (Schumm et al., 1995); these properties make this field site ideal to study the influence of groundwater seepage in isolation from factors that typically influence confluence geometry. An example of such a confluence is shown in Figure 3-2. These streams are roughly ~ 20 cm in width and ~ 1 cm in depth (Devauchelle et al., 2010).

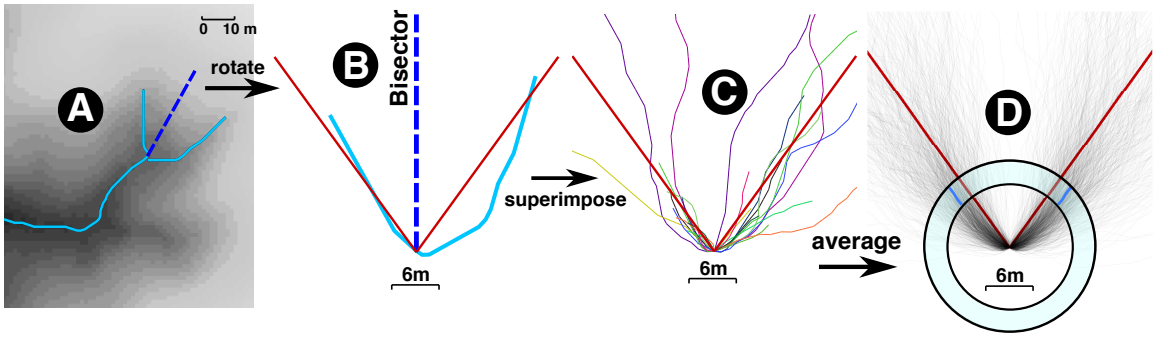

Figure 3-3: (a) A first-order confluence, (b) rotated along its bisector, with (c) a few of these streams superimposed. (d) All 1225 first-order confluences shown in grey, set against 72° lines in red. We illustrate the averaging scheme in the annulus: we take radial slices from confluence junctions and average the polar angle for each stream within these slices. (e) Average shape of these 1225 confluences (light blue; standard deviation of angle in dark blue), against a 72° confluence (red). The individual channels are superimposed in grey. Each point along the trajectory here represents the average of 1300 points. A small resolution anomaly occurs in these averaging schemes close to the junction due to the limit of our grid resolution (1.2 m) and should be neglected. (f) The same data from (a) transformed to polar coordinates to demonstrate the behavior of the polar coordinate θ as measured from the junction. The anomaly described over the first 1.2 meters is omitted for clarity.

We extracted the location of streams in Florida by thresholding the curvature of topographic contours, obtained from laser altimetry data with a horizontal resolution of 1.2 m and a vertical resolution of about 5 cm (Devauchelle et al., 2012), as outlined by Devauchelle et al. (2010). We ordered our channels according to Horton-Strahler ordering (Horton, 1945; Strahler, 1952) and aligned first-order confluence pairs along their bisector, as determined by the sum of the vectors obtained from regression of each of the two confluent streams. To obtain angle as a function of distance from the junction, the aligned channel coordinates were converted to polar coordinates, and angle was averaged for each stream as a function of distance from the junction, as illustrated in Figure 3-3(a)-(d). A network-wide averaging of 1225 confluences from our field site by this method is shown in Figure 3-3, where each point represents an average of points within a radial slice. The shape exhibits a wide angle deviation from the predicted 72° angle near the junction. We note that this averaging scheme is not necessarily representative of the archetypal groundwater-fed stream confluence shape, but a visualization of where channels are located on average.

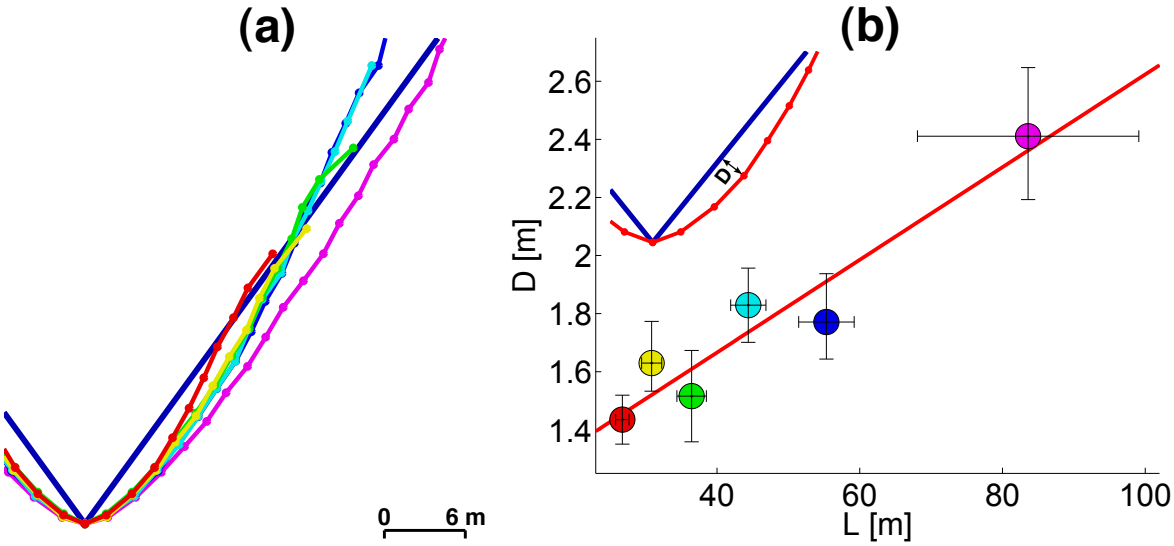

Figure 3-4: (a) spatially averaged curves (binned by the same mechanism as in Figure 3-3). Each point represents the average of 250 points. (b) the maximum distance D from the 72° lines against the average length L of these streams. The error bars in L indicate the standard deviation and the error bars in D indicate standard error of the mean. The inset on the top left illustrates the measurement D.

There are three symmetric geometric adjustments that may give rise to this wide angle deviation: (1) headward growth in a direction that follows the deviant trajectory, (2) movement (advance) of the junction, or (3) lateral migration of the channel after growth. We hypothesize that the lateral migration of channels is responsible for the deviation from 72° we observed in Figure 3-3. The average channel location therefore represents a balance between migrational forcing and confinement by valley sidewalls. We therefore assume that Figure 3-3 represents a statistical steady-state configuration.

We repeat the averaging scheme of Figure 3-3 for channels sorted by arclength between spring and junction, precluding particularly small (< 25 m) and large (> 120 m) channels from this analysis. Channels averaged in this manner are shown in Figure 3-4, where different average channel lengths correspond to different colors. As channel length increases, the size of the deviation from the 72° lines increases, which suggests that the strength of confinement decreases with channel length. This is consistent with confinement caused by diffusion of the valley sidewalls, which are steepest near the springs.

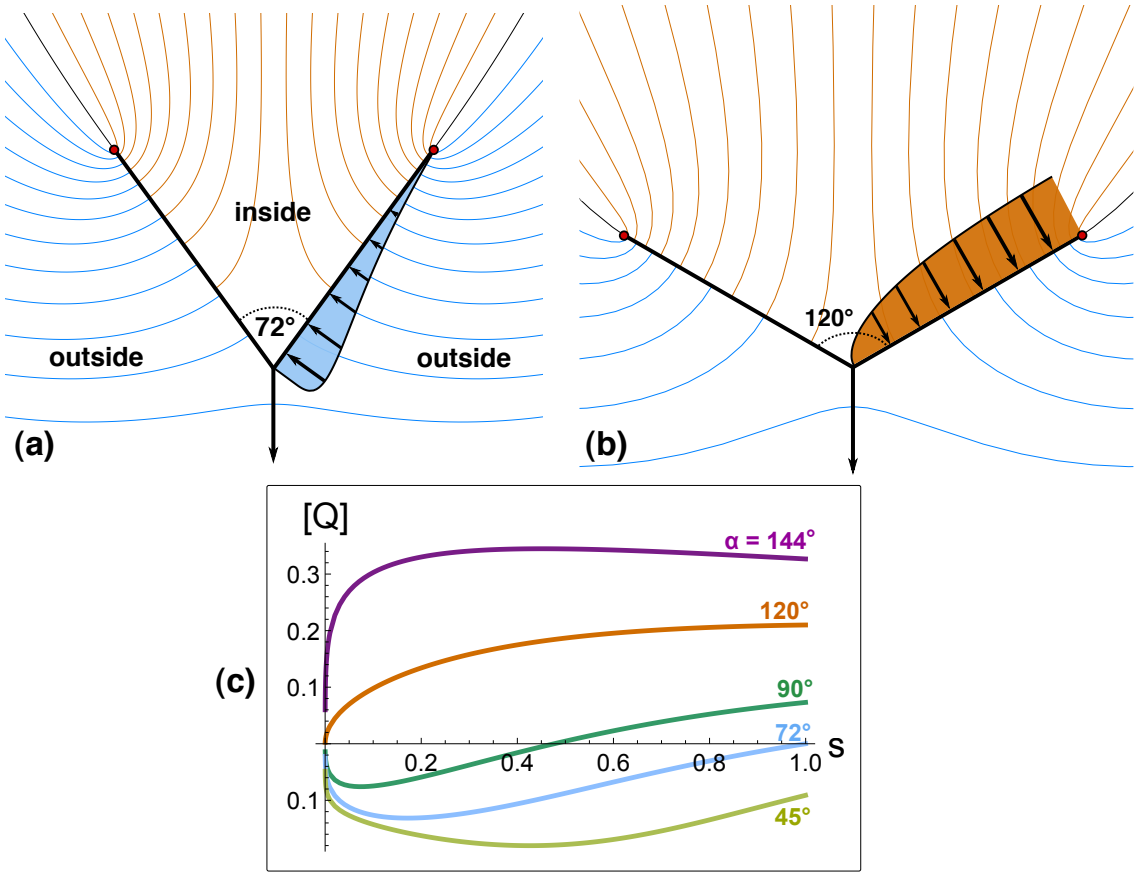

Figure 3-5: (a) Illustration of the flux asymmetry into stream confluences branching at an angle of 72°. The density of streamlines indicates the flux density. The uneven streamline spacing downstream of the tips suggests that the field is asymmetric. The shaded region is the difference between the fluxes into these two sides, indicating that the flux is larger on the shaded side. The orange and blue colors indicate association with the inside of the angle and the outside, respectively. (b) The same illustration as (a) but with a confluence angle of 120°. (c) Flux jump $[Q]$ as a function of arclength measured from the junction s (rescaled by length of the branch) for Y-shaped confluences of varying confluence angle α.

3.3.2 A mechanism for lateral migration

We hypothesize that forcing from an asymmetric groundwater field downstream is responsible for this lateral stream migration, as streams adjust to the flux difference from their two sides. While self-similar branches with a 72° angle between them have a locally symmetric field around their tips, this field is not symmetric downstream from the tips. An illustration of this asymmetry is shown in Figure 3-5(a). Consider again the confluence geometry in which the two confluent streams are finite and

mirror symmetric about a third, semi-infinite stream downstream. Let α be the angle between these two finite branches. Denote the region between them as the "inside" and the regions between each branch and the semi-infinite branch as "outside," as labelled in Figure 3-5(a). We reference these two regions with the subscripts i and o, respectively. The flux from the inside is therefore $Q_i(s)$ and, from the outside, $Q_o(s)$, where s is the arclength measured from the junction. We define the *flux jump* $[Q(s)]$ as

$$[Q(s)] = Q_i(s) - Q_o(s). \tag{3.4}$$

Symmetry arguments provide some intuition about the geometry that migration according to $[Q(s)]$ would produce. When $\alpha = 72°$, the field is locally symmetric (Cohen et al., 2015) and so $[Q(s)] = 0$ at the tips. Therefore, no lateral migration would occur at the tips. Close to the junction, the two confluent streams appear infinitely long, becoming locally indistinguishable from the second-order, infinitely long downstream channel. When $\alpha = 120°$ and all three branches are infinitely long, the field will be symmetric on either side of the channel, producing flux jump $[Q_0] = 0$ everywhere. When the confluent streams are finite, $[Q(s)]$ increases most slowly with s when $\alpha = 120°$ (see Appendix 3.A for proof). Consequently, the flux jump near the junction is minimized when $\alpha = 120°$, and the angle $\alpha = 120°$ can be understood as the most stable angle near the junction. We therefore hypothesize that real channels that migrate according to this flux jump exhibit a $\sim 120°$ angle near the junction and a $\sim 72°$ angle near the tips. These predictions agree with the angles of real confluences near the junction and tips, respectively, shown in Figure 3-3(f).

The flux-dependent migration process we have discussed thus far can be approximated by

$$v_m(s) = \epsilon[Q(s)] - \nu\kappa(s), \tag{3.5}$$

where $[Q(s)]$ is the flux jump across the river at an arclength s with units of m (this flux is the Poisson flux, which is the flux in m^2/s divided by precipitation rate (Petroff et al., 2011)), v_m is the perpendicular velocity at which the channel is migrating, $\epsilon > 0$ is a constant with units s^{-1}, $\nu > 0$ is a constant with units m^2/s and κ is the local

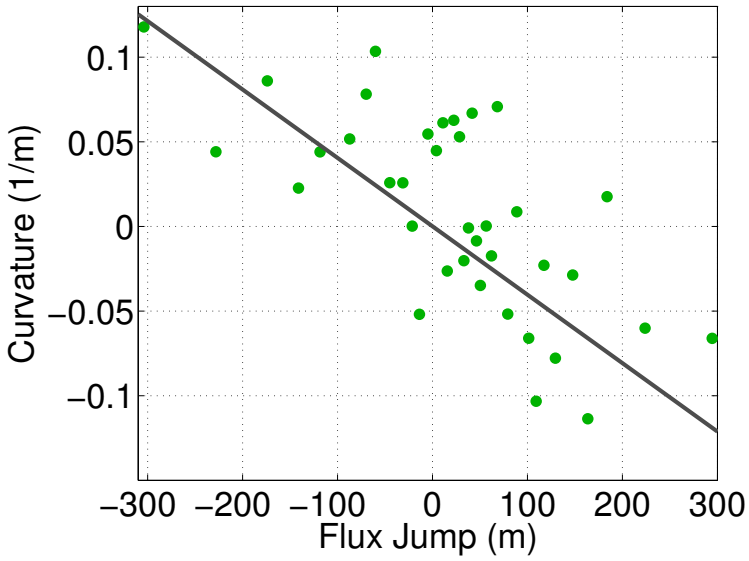

Figure 3-6: Curvature against flux jump for first-order confluences. The dark grey line is a fit of slope -4×10^{-4}. Each green point represents the average of 10 points.

curvature (Weisstein, 2017a). The $\nu\kappa$ term represents a stabilizing effect that can be understood as a first-order approximation to the influence of soil creep as streams migrate against the valley wall. If this stabilization is balanced by the flux difference across the stream and the streams are in a statistical steady state, we have

$$v_m = 0 \implies \frac{[Q(s)]}{\kappa(s)} = \frac{\nu}{\epsilon}. \tag{3.6}$$

The ratio of $[Q]$ to κ therefore predicts a ratio ν/ϵ with units of m^2. Physically, this ratio represents the difference in area drained on either side over the length of the curve. We calculate $[Q]$ and κ for a number of first-order confluences in our network, shown in Figure 3-6. We restrict this measure to a portion of the network for which we have LIDAR data that can clearly resolve curves in these streams. The slope of the line predicts the ratio $\nu/\epsilon \approx 2474$ m^2.

3.4 Network migration

3.4.1 Network-wide power spectrum

We now seek to determine the effect of groundwater on the migration of the entire channel network. In what follows, we determine the periodicity of network-wide fluctuations in curvature. A representative channel colored by curvature is shown in Figure 3-7.

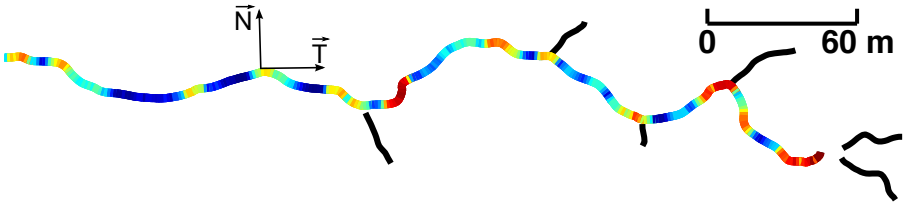

Figure 3-7: A second-order channel colored by curvature.

Determining the periodicity of stream curvature requires a rotation-invariant, differential representation of the geometry. To this end, we rewrite our signal in terms of the 2D Frenet equations. The Frenet equations fully describe the relationship between tangent vectors, normal vectors, and curvature on a twice continuously differentiable curve (Kühnel, 2015):

$$\frac{d\vec{T}}{dt} = \kappa\vec{N}, \tag{3.7}$$

$$\frac{d\vec{N}}{dt} = -\kappa\vec{T}, \tag{3.8}$$

where $\vec{T}$ and $\vec{N}$ are the tangent and normal vectors to the curve. We calculate the tangent vector over 3 meters (as determined by the vector drawn between the two points surrounding the point in question) and curvature over 5 meters for each point in all first-order channels, to obtain the $d\vec{N}/dt$. No additional information in carried in $d\vec{T}/dt$, so we can use $d\vec{N}/dt$ without loss of generality. We write the tangent vector $\vec{T}$ as a single imaginary number $T_x + iT_y$, where T_x and T_y are the x and y components of $\vec{T}$, and $i^2 = -1$. Equation (3.8) becomes

$$\frac{d\vec{N}}{dt} = -\kappa(T_x + iT_y). \tag{3.9}$$

The averaged power spectra of (3.9) for channels of all orders in our network is shown in Figure 3-8. The power spectrum of (3.9) is roughly equivalent to the power spectrum of κ alone, but the sign of the frequency spectrum also indicates whether the channel is generally moving counterclockwise (positive) or clockwise (negative) as one travels downstream from the tip. The global effect of this bias is reflected in the slight asymmetry of Figure 3-8(a). Positive and negative frequencies are combined in Figure 3-8(b) and in subsequent figures.

We now calculate the power spectra separately for first-, second-, and third-order channels and average them, shown in Figure 3-8(c). We only use streams longer than 50 meters for this calculation, to diminish the effect of the length distribution on the power spectra. Stream curvatures in our network appear to fluctuate at a dominant frequency that corresponds to a wavelength of 26.7 m for first-order channels, 28.3 m for second-order channels, and 28.4 for third-order channels. The higher power spectral density of the second and third-order channels results from higher values of curvature in second-order channels. However, because a higher value of curvature generates an increased wavelength by simply extending the channel arclength, the correspondence of first-order and second-order channel curvature wavelengths may be even closer than we have found. The agreement of this $\sim$ 30 m wavelength to the length scale over which the wide opening angle of confluences returns to the 72° lines (seen in the intersection between the light blue and red lines in Figure 3-3(f)) suggests that both network-wide fluctuations in curvature and confluence migration may be influenced by a common mechanism.

This spectral analysis resembles analyses conducted on river meanders, which form as flowing water erodes river banks and redeposits eroded sediment downstream (Speight, 1965; Hooke, 1984; Gutierrez et al., 2014). However, we contend that the distinct morphology of the streams we study here suggests that they were shaped by different processes than those typically attributed to the formation of river meanders. For meanders confined by valley walls, the meander wavelength is $\sim$ 17 times larger than the width of the meandering river (Nicoll and Hickin, 2010). In contrast, first-order channel widths in the Bristol, Florida network range from $\sim 10 - 20$

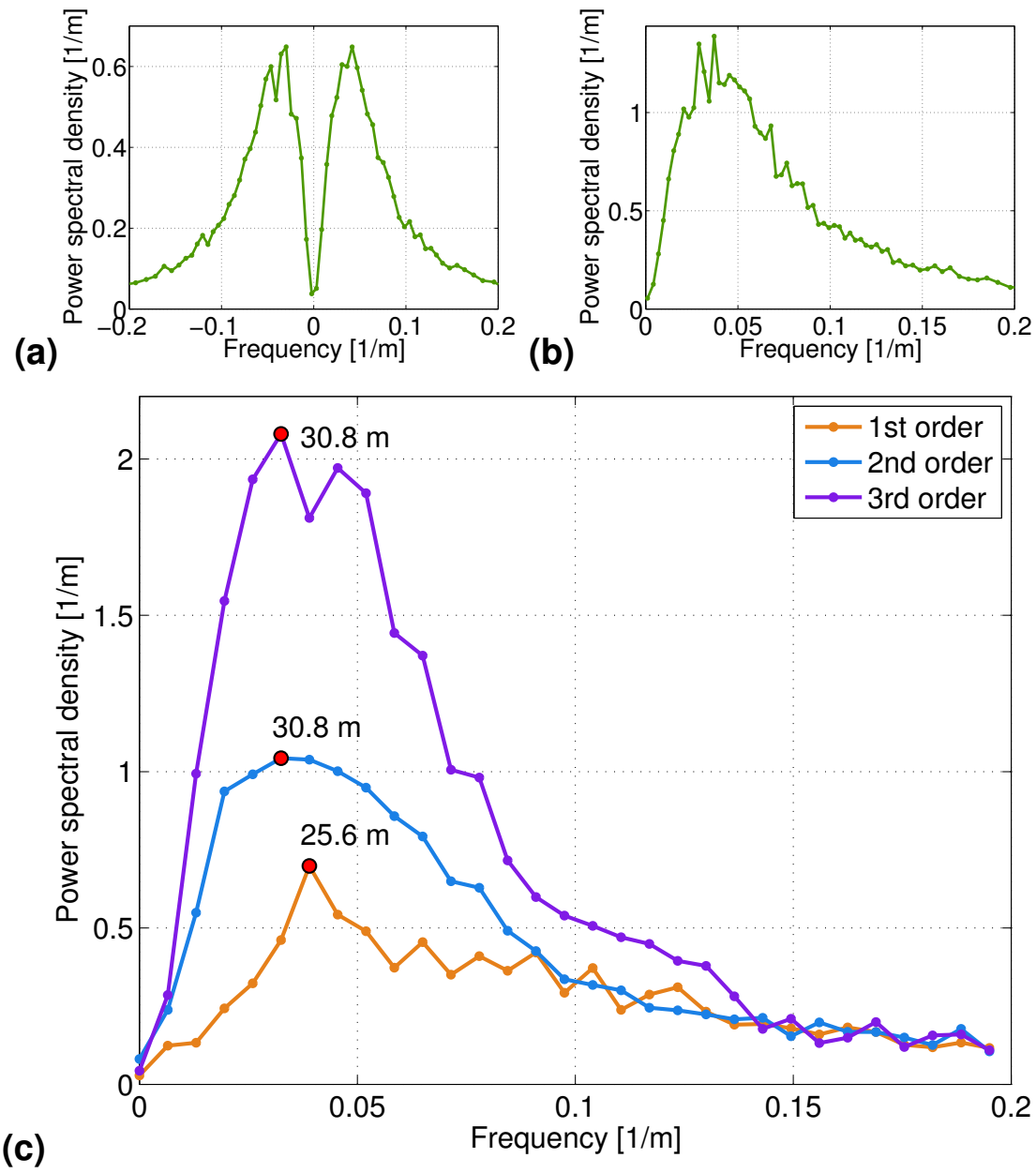

Figure 3-8: (a) The averaged power spectrum of channels (all orders) in the Bristol, Florida network. The asymmetry reflects a tendency of channels to turn clockwise (negative frequencies) or counterclockwise (positive) from the tip. Each point represents the average of 300 points. The black line reflects the average of points within evenly spaced bins along the frequency axis. (b) The same data as (a), symmetrized. (c) The averaged power spectrum of $\frac{d\vec{N}}{dt}$ for first-order channels in orange, second-order channels in blue, and third-order channels in purple. Each point represents 150 averaged points. The red outlined dots indicate the peaks of these curves, labelled with the corresponding periodicity in meters.

cm near the springs up to 50 cm near downstream confluences, producing a ratio of wavelength to channel width of $\sim$ 50-500. Streams in this network also have a sinuosity (defined as the ratio of channel length to valley length) < 1.3, which would generally be classified as "straight", rather than "meandering" (Bierman and Montgomery, 2013). We therefore suggest that the fluctuations reflected in Figure 3-8 are not primarily the result of erosional dynamics typically associated with river meanders, though the increased curvature in higher order streams may signify an increasing importance of typical meandering dynamics downstream. However, the independence of curvature wavelength with order suggests that this length scale is initially set by factors independent of dynamics within the streams and only later augmented by such dynamics, if at all.

3.4.2 Evidence of network-wide migration

We now present field evidence that these channels are indeed migrating in the manner we suggest. First, we measure slope asymmetries along the valley sidewalls, which we define as the valley sidewall slope on one side subtracted from the other. We hypothesize that, if channels are laterally migrating, they should steepen the sidewall which they migrate into. We next show that curvature and flux jump are related across the entire network, suggesting that all streams are in a statistical steady state.

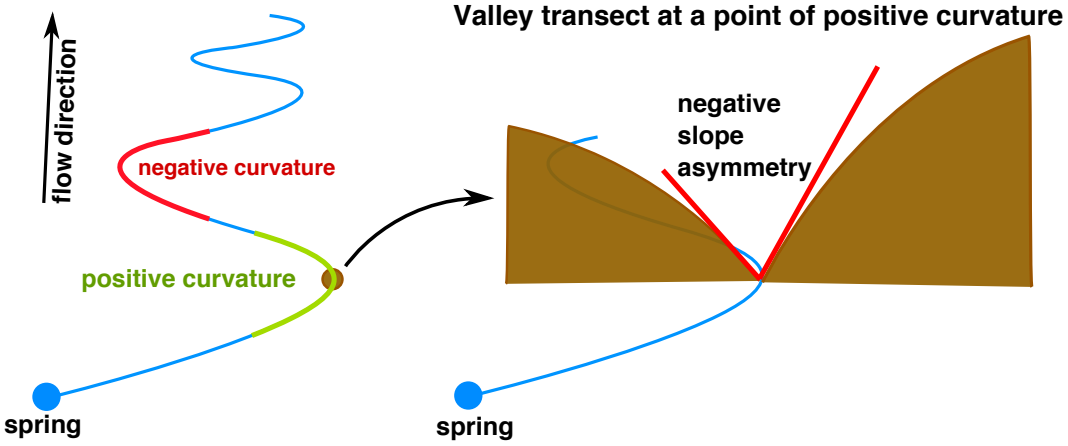

Figure 3-9: An illustration of the physical interpretation of the sign of curvature and slope asymmetry, as defined in the text.

We quantify the slope asymmetry by extracting the channel direction over a window of four meters along all channels in the network. We then obtain values of slope over 10 meters on either side of the channel along the axis perpendicular to this direction from LIDAR data. We take the steepest 20% of these slopes and average them, under the assumption that the steepest sections of a valley represent the steepest steady state configuration sustainable by a balance between sediment transport and diffusive transport. Facing downstream, we call the averaged slope to the left of the stream S_l and to the right, S_r. We then calculate the slope asymmetry, which we define as $(S_l - S_r)/(S_l + S_r)$. This quantity is therefore positive when the steeper slope is on the left and negative when on the right.

We compare slope asymmetry, curvature, and flux difference $((j_l - j_r)/(j_l + j_r)$, where j is flux). First, the relationship between slope asymmetry and curvature is shown in Figure 3-10(a). A negative curvature indicates a negative second-derivative: facing downstream, this corresponds to a channel that rotates counter-clockwise. The signs of curvature and slope asymmetry are illustrated in Figure 3-9. Negative values of curvature appear to correspond to positive values of slope asymmetry, suggesting that the valley side into which a channel veers has a higher slope. Second, the data for flux jump against slope asymmetry is shown in Figure 3-10(b), which scale linearly. This suggests that the steeper side of the valley tends to draw greater groundwater flux. These results are consistent with our hypothesis that streams migrate, steepening the topography as they do.

Finally, in Figure 3-10(c), we find that curvature and flux jump are also related, which suggests that the network-wide curvature wavelength is a product of the same flux- and curvature-dependent migration process responsible for the wide opening angle of confluence junctions. The fit line in Figure 3-10(c) corresponds to a value of $\frac{\nu}{\epsilon} \approx 739$ m^2, which represents the difference in area drained into each side of a channel over the length of the curving region.

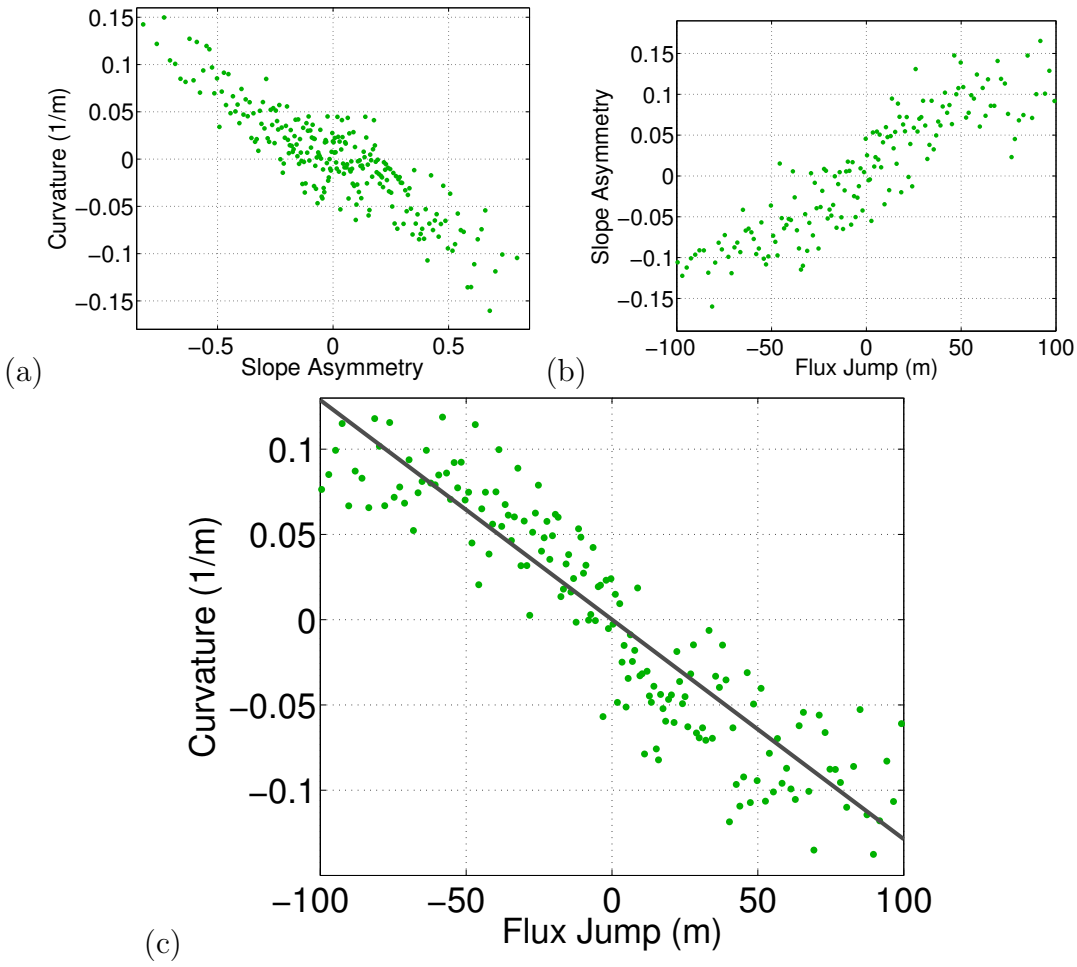

Figure 3-10: For all plots, each point is the average of 100 points. (a) Curvature against slope asymmetry, as defined by $(S_l - S_r)/(S_l + S_r)$, where S_l and S_r are the slopes to the left and right of the stream, respectively, when facing downstream. (b) Slope asymmetry against flux jump, $(\phi_l - \phi_r)/(\phi_l + \phi_r)$, where ϕ_l and ϕ_r are the fluxes from the left and the right of the stream, respectively, when facing dowstream. (c) Curvature against flux jump. The dark grey line corresponds to a slope of -0.0013 or a value of $\nu/\epsilon \approx 769$ m^2.

3.5 Conclusion

We have presented evidence that stream migration can occur in response to an asymmetric groundwater table. We suggested that this migration is responsible for two planform features: a wide confluence angle and a network wide curvature fluctuation along the reach. First, we presented theoretical results that suggest that confluence migration according to this asymmetry would favor a symmetric configuration with

a 120° angle near stream junctions, narrowing to a 72° angle near stream tips. We found evidence of such a feature in real streams. Second, we found that network-wide river curvature fluctuates with a period comparable to the length scale of this deviation, and we presented topographic evidence that suggests that this fluctuation is a product of the same migration mechanism. Additional research may reveal the extent to which groundwater field asymmetries are responsible for widespread river migration in groundwater-fed environments.

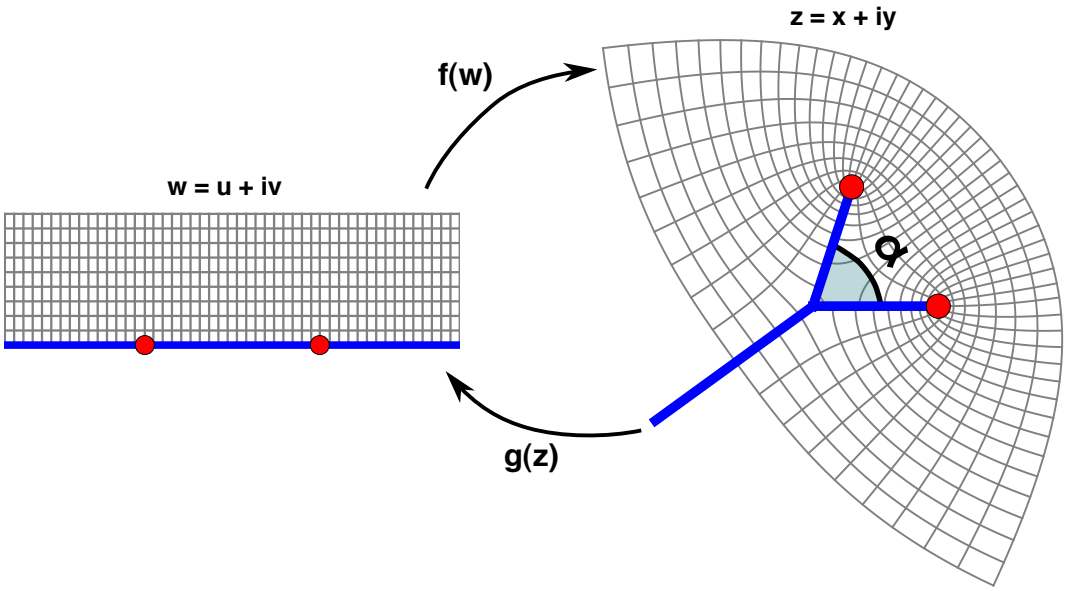

Figure 3-11: An illustration of the map from the upper half plane $w = u + iv$ to the physical plane $z = x + iy$ given by equation (3.10). The map has a single parameter $c = \alpha/2\pi$, where α is the angle between the two branches.

3.A Optimal migration angle

3.A.1 Conformal map

The general form of the conformal map which produces the fishtail shape in Figure 3-1 is

$$f(w) = w^{2c}\left(\frac{1}{c} - w^2\right)^{1-c}, \tag{3.10}$$

where c is the angle (α) between the two branches as a fraction of 2π. $f(w) : w \to z$ maps from the upper half plane, $w = u + iv$, to the physical plane $z = x + iy$. Because the Laplace equation 3.3 is conformally invariant, then the imaginary part of $f^{-1}(z) = g(z) : z \to w$ is harmonic and provides us with the shape of the groundwater field around the bifurcated geometry. This map is illustrated in Figure 3-11.

3.A.2 Flux

While we cannot invert $f(z)$ directly, we can calculate the flux jump implicitly in terms of the mathematical variable v by choosing a rotation of the map such that

one of the branches lies along an axis. Conveniently, this is the case for (3.10), for which one branch lies along the positive x axis, as shown in Figure 3-11. The flux into this branch is therefore dv/dy, where v is the imaginary part of w. To this end, the derivative dz/dv is given by

$$\frac{\partial z}{\partial v} = 2ic\left(\frac{1}{c} - w^2\right)^{1-c} w^{2c-1} - 2i(1-c)\left(\frac{1}{c} - w^2\right)^{-c} w^{2c+1}. \tag{3.11}$$

And $\partial y/\partial v$ is the imaginary component of this quantity evaluated at $v = 0$:

$$\frac{\partial y}{\partial v} = -2Re\left(u^{2c-1}\left(\frac{1}{c} - u^2\right)^{-c}(u^2-1)\right). \tag{3.12}$$

If $0 < u \leq \frac{1}{\sqrt{c}}$, which is the range along the x-axis we are concerned with, the argument within Re is always real. The flux Q within this domain is given by the reciprocal of this quantity:

$$Q = \frac{\partial v}{\partial y} = -\frac{2}{u^{2c-1}\left(\frac{1}{c} - u^2\right)^{-c}(u^2-1)} \tag{3.13}$$

The flux jump is therefore implicitly defined by (3.10) and (3.13). An illustration of the resulting behavior for a few values of c is shown in Figure 3-5(c).

3.A.3 Flux jump as $x \to 0$

Q exhibits a peculiar behavior: the flux Q and, consequently, the flux jump $[Q]$ go to 0 regardless of the choice of c. To demonstrate this analytically, we can calculate the limit of (3.13) as $u \to 0, \frac{1}{\sqrt{c}}$, the roots that correspond to the junction. First, in the limit $u \to 0$,

$$\lim_{u\to 0} Q = \lim_{u\to 0} \frac{2}{u^{2c-1}c^c} \tag{3.14}$$

$$= 0, \tag{3.15}$$

assuming $c < 1/2$ (the bifurcation angle is less than π). Similarly, for $u \to \frac{1}{\sqrt{c}}$,

$$\lim_{u\to\frac{1}{\sqrt{c}}} Q = \lim_{u\to\frac{1}{\sqrt{c}}} \frac{-2\left(\frac{1}{c}-u^2\right)^c}{c^{\frac{2c-1}{2}}\left(\frac{1}{c}-1\right)} \tag{3.16}$$

$$= 0, \tag{3.17}$$

assuming $c > 0$ (the bifurcation angle is greater than 0). The flux jump therefore also approaches 0 for all values of c as $x \to 0$.

3.A.4 Flux jump departs from 0 most slowly for $\alpha = 2\pi/3$

We seek to determine the rate at which flux jump departs 0 from the junction as a function of $c = \alpha/2\pi$. This can be found by solving $\frac{\partial^2 v}{\partial x \partial y} = 0$ for c. To this end, recall that ∂_z, the partial derivative with respect to z, and ∂_z^2 can be written in terms of x and y as

$$\partial_z = \frac{1}{2}\left(\partial_x - i\partial_y\right) \tag{3.18}$$

$$\partial_z^2 = \frac{1}{4}\left(\partial_x^2 - 2i\partial_x\partial_y + \partial_y^2\right). \tag{3.19}$$

The derivative $\frac{\partial^2 v}{\partial x \partial y}$ can therefore be rewritten in terms of z as

$$\frac{\partial^2 v}{\partial x \partial y} = -\frac{1}{2} Im\left(\frac{\partial^2 v}{\partial z^2}\right). \tag{3.20}$$

However, we only have $\partial v/\partial z$ in terms of u and v. We therefore require this expression to be rewritten in terms of $\partial^2 z/\partial^2 v$, which we can now calculate directly:

$$\frac{\partial^2 v}{\partial x \partial y} = -\frac{1}{2} Im\left(\frac{\partial^2 v}{\partial z^2}\right) \tag{3.21}$$

$$= \frac{1}{2} Im\left(\frac{\frac{\partial^2 z}{\partial v^2}}{\left(\frac{\partial z}{\partial v}\right)^3}\right). \tag{3.22}$$

We are only concerned with $w = u$, for $0 < u < \frac{1}{\sqrt{c}}$. Therefore,

$$\frac{\partial Q}{\partial x} = \frac{\partial^2 v}{\partial x \partial y} = \frac{1}{2} \frac{\left(\frac{1}{c} - u^2\right)^{2c} (a + b + c + d)}{\left(2c\left(\frac{1}{c} - u^2\right) u^{2c-1} - 2(1-c)u^{2c+1}\right)^3}, \tag{3.23}$$

where

$$a = 4(1-c)cu^{2c} \tag{3.24}$$

$$b = 2(1-c)(1+2c)u^{2c} \tag{3.25}$$

$$c = 2c(1-2c)\left(\frac{1}{c} - u^2\right) u^{2c-2} \tag{3.26}$$

$$d = 4(1-c)c\left(\frac{1}{c} - u^2\right)^{-1} u^{2+2c}. \tag{3.27}$$

We want $\partial_x[Q(x)] = \partial_x(Q(u_1(x)) + Q(u_2(x)))$ as a function of c as x approaches its roots, where $f(u_1) = x$ and $f(u_2)$. To this end, we invert the conformal map (3.10) in the limit as u approaches its roots, $u \to 0, \frac{1}{\sqrt{c}}$. Because we are dealing only with values on the real axis both in the mathematical and physical plane, we let $v = 0$ for equation (3.10). For small u, x is given by

$$x = f(u) = u^{2c}\left(\frac{1}{c} - u^2\right)^{1-c} \tag{3.28}$$

$$\approx u^{2c} c^{c-1}. \tag{3.29}$$

Similarly for $u \to 1/\sqrt{c}$,

$$x = f(u) = u^{2c}\left(\frac{1}{c} - u^2\right)^{1-c} \tag{3.30}$$

$$\approx c^{-c}\left(\frac{1}{c} - u^2\right)^{1-c}. \tag{3.31}$$

Inverting equations (3.40) and (3.42) gives us the two values of u that correspond to a single value of x,

$$u_1 = \left(\frac{x}{c^{c-1}}\right)^{\frac{1}{2c}}, \; u_2 = \sqrt{\frac{1}{c} - x^{\frac{1}{1-c}} c^{\frac{c}{1-c}}}. \tag{3.32}$$

We combine equations (3.43) and (3.23) to obtain $\partial_x[Q(x)]$ explicitly for small x:

$$\partial_x[Q(x)] \approx \left.\frac{\partial Q}{\partial x}\right|_{u=\left(\frac{x}{c^c-1}\right)^{\frac{1}{2c}}} + \left.\frac{\partial Q}{\partial x}\right|_{u=\sqrt{\frac{1}{c}-x^{\frac{1}{1-c}}c^{\frac{c}{1-c}}}}. \tag{3.33}$$

Substituting these values in, we obtain an expression for $\partial_x[Q(x)]$ for small x:

$$\partial_x[Q(x)] \approx -\underbrace{\left(\frac{c^{\frac{1}{1-c}+\frac{1}{2}}}{4(c-1)^2}\right)}_{\alpha} x^{\frac{1}{1-c}-2} + \underbrace{\left(\frac{1}{8}c^{\frac{1}{2}\left(\frac{1}{c}-5\right)}(1-2c)\right)}_{\beta} x^{\frac{1}{2c}-2}. \tag{3.34}$$

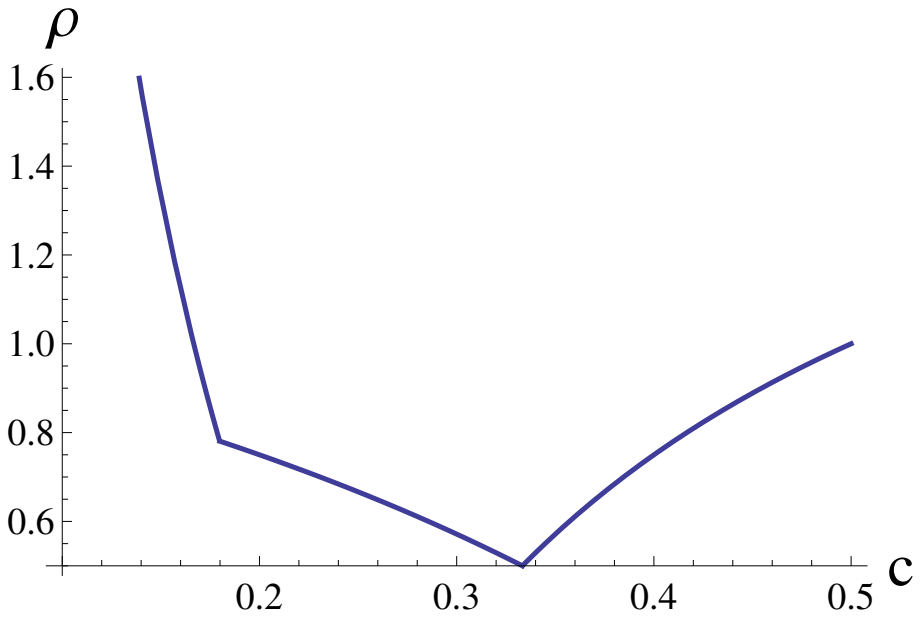

Figure 3-12: A plot of $\rho(c)$, as defined in equation (3.37).

To understand the behavior of this function, note that within the range $0 < c < 1/2$, both α and β are positive. Since we are concerned with the behavior of (3.34) in the vicinity of $c = 1/3$, we happily restrict ourselves to this range. For values on either side of $c = 1/3$, we have

$$\partial_x[Q(x)] \approx -\alpha x^{\frac{1}{1-c}-2} \to -\infty \text{ for } c < 1/3 \text{ as } x \to 0 \tag{3.35}$$

$$\partial_x[Q(x)] \approx \beta x^{\frac{1}{2c}-2} \to +\infty \text{ for } c > 1/3 \text{ as } x \to 0. \tag{3.36}$$

Therefore, $c = 1/3$ represents a special point for which the rate at which flux jump increases with x near the junction is at a minimum. This can be seen by considering the quantity

$$\rho(c) = \max\left(\frac{1}{1-c} - 2,\ \frac{1}{2c} - 2\right) \tag{3.37}$$

where equation (3.36) for small x behaves as

$$\partial_x[Q(x)] \approx x^{\rho(c)}. \tag{3.38}$$

$\rho(c)$ is shown in Figure 3-12, and as expected by our reasoning above, ρ has a minimum at $c = 1/3$, for which $\partial_x[Q[x]] \sim 1/\sqrt{x}$.

3.B Extra-manuscript appendix

The following derivation was not included in the manuscript of the published paper, but may be of interest to the reader, and so is included here. In it, we offer an alternative way to view the flux jump at a confluence angle of $2\pi/3$ – as the angle at which the flux jump infinitesimally close to the origin changes sign.

3.B.1 Flux jump changes sign at $\alpha = 2\pi/3$

We briefly include here a derivation not included in the published paper as it provides an alternate way of viewing the symmetry of the angle $\alpha = 2\pi/3$. This proof is also conceptually simpler than the derivation of the flux jump derivative with respect to x.

The symmetry of $2\pi/3$ can alternatively be found by noticing that the flux jump appears to change sign between $2\pi/3$ and $\pi/2$. We therefore seek the critical angle α_c at which this occurs. To this end, we take (3.10) in the limit as u approaches its roots, $u \to 0, \frac{1}{\sqrt{c}}$. Because we are dealing only with values on the real axis both in the mathematical and physical plane, we let $v = 0$ for equation (3.10). For small u,

x is given by

$$x = f(u) = u^{2c}\left(\frac{1}{c} - u^2\right)^{1-c} \tag{3.39}$$

$$\approx u^{2c}c^{c-1}. \tag{3.40}$$

Similarly for $u \to 1/\sqrt{c}$,

$$x = f(u) = u^{2c}\left(\frac{1}{c} - u^2\right)^{1-c} \tag{3.41}$$

$$\approx c^{-c}\left(\frac{1}{c} - u^2\right)^{1-c}. \tag{3.42}$$

Inverting equations (3.40) and (3.42) gives us the two values of u that correspond to a single value of x,

$$u_1 = \left(\frac{x}{c^{c-1}}\right)^{\frac{1}{2c}},\ u_2 = \sqrt{\frac{1}{c} - x^{\frac{1}{1-c}}c^{\frac{c}{1-c}}}. \tag{3.43}$$

Combining equations (3.40), (3.42), and (3.13), we obtain an expression for flux jump $[Q(x)]$ for small x:

$$[Q(x)] \approx -\underbrace{\frac{c^{\frac{1+c}{2-2c}}}{2(1-c)}}_{A}x^{\frac{c}{1-c}} + \underbrace{\frac{1}{2c^{\frac{3}{2}-\frac{1}{2c}}}}_{B}x^{\frac{1}{2c}-1} \tag{3.44}$$

Notice that within the range $0 < c < 1/2$ (corresponding to a slit or an opening angle of π), the quantities A and B are both positive. And as long as we are not infinitely close to $c = 0$ or $c = 1/2$, they remain finite, which is acceptable as we are only concerned with values near $c = 1/3$. Equation (3.44) can be rewritten as

$$[Q(x)] = -Ax^{\frac{c}{1-c}} + Bx^{\frac{1}{2c}-1} \tag{3.45}$$

Notice that $\lim_{x\to 0}[Q(x)] = 0$, and therefore this solution agrees with (3.15) and (3.17).

If instead, however, we choose a value of x that it is infinitesimally small, but non-zero, only one of the terms $-Ax^{\frac{c}{1-c}}$ or $Bx^{\frac{1}{2c}-1}$ will dominate for $c \neq 1/3$. Moreover,

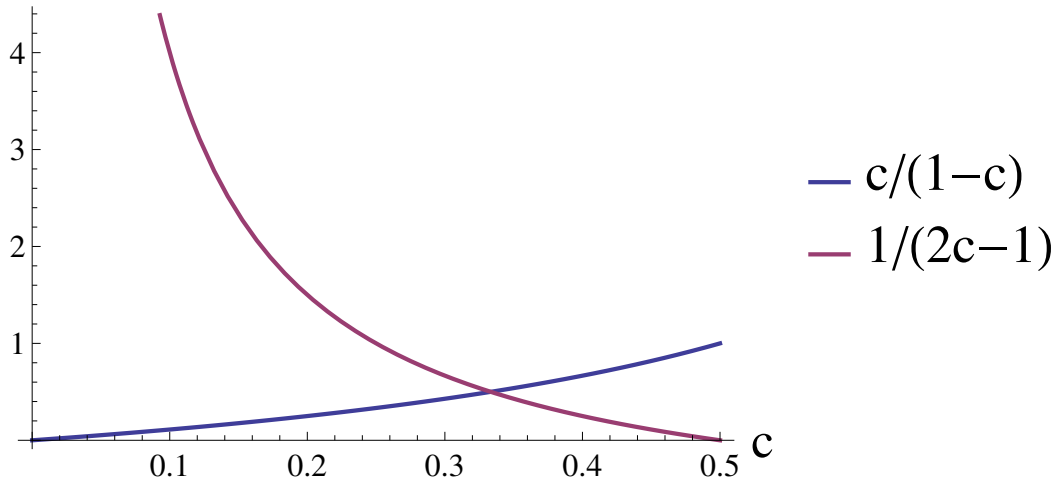

Figure 3-13: A comparison of two exponents $\frac{c}{1-c}$ and $\frac{1}{2c-1}$ as functions of c. The functions intersect at $c = 1/3$, which is the crossover point at which one exponent overtakes the other in equation (3.45).

the exponent $\frac{c}{1-c}$ is monotonic increasing and $\frac{1}{2c} - 1$ is monotonic decreasing within the domain $0 < c < 1/2$, and the two curves intersect at $c = 1/3$, as shown in Figure 3-13. Consequently, for values of c infinitesimally less than $1/3$, $[Q(x)]$ will be negative near $x = 0$, and for values of c infinitesimally larger than $1/3$, $[Q(x)]$ will be positive near $x = 0$. $c = 1/3$ represents the angle at which the flux jump changes sign for non-zero x close to the junction.

Chapter 4

Shapes of river networks

Abstract

River network scaling laws do not universally adhere to those predicted by any single existing dynamical model. Here we show that these scaling laws vary systematically with the climatic aridity index. We find that arid basins do not change their proportions with size, while humid basins do. To explore why, we study an aspect ratio $L_\perp/L_\parallel$ between basin width $L_\perp$ and basin length $L_\parallel$. We find that this ratio also exhibits a dependence on climate, and we argue that this ratio can be understood as a structural expression of the confluence angle. Finally, we find that in humid basins, this ratio decreases with basin size, which we argue is a geomorphological manifestation of a common hydrogeological hierarchy. Our results offer an explanation of the origin of variability in common network scaling exponents and suggest that the absence of self-similarity in humid basins indicates the presence of characteristic hydrological scales.

4.1 Introduction

River networks form stunning branching patterns that repeat over many scales. In recent years, their seemingly fractal appearance has led to study in the context of simple unifying dynamics that operate independent of scale (Tarboton et al., 1988;

Rodríguez-Iturbe and Rinaldo, 2001; Dodds and Rothman, 2000). Perhaps the conceptually simplest of these is the random walk model introduced by Scheidegger (1967), who suggested river flow direction could be approximated as a random downhill choice on a lattice. A number of other simple models have also been devised, providing new ways of interpreting river network formation. For example, a simple loosening of the downhill condition of the Scheidegger model (a random walk on a lattice in one of eight directions, rather than two or three) produces a network with different scaling properties (Manna et al., 1992). Similarly, a class of optimal channel network models (Rinaldo et al., 1993; Rodríguez-Iturbe and Rinaldo, 2001) suggested that river networks self-organize to an energetically optimal state, bearing qualitative similarity to avalanches and other so-called self-organized critical processes (Bak et al., 1987). Ultimately, study of such models revealed how scaling laws delineate distinct morphological classes of river networks (Dodds and Rothman, 2000; Maritan et al., 1996). However, real river dynamics and forms are often subject to a wide range of geological and environmental constraints (Bierman and Montgomery, 2013), producing changes in the way they branch, flow, and self-organize. These constraints inevitably introduce variability into network scaling laws and have stymied efforts to develop a unifying theory (Dodds and Rothman, 2000; Stankiewicz and De Wit, 2005; Willemin, 2000).

Here we ask how exponents of these network scaling laws can be understood through both an environmental gradient – the local aridity – and the simple physical models we have introduced. We then consider how these scaling laws can be understood explicitly through study of basin shape and its dependence on local aridity and length scale.

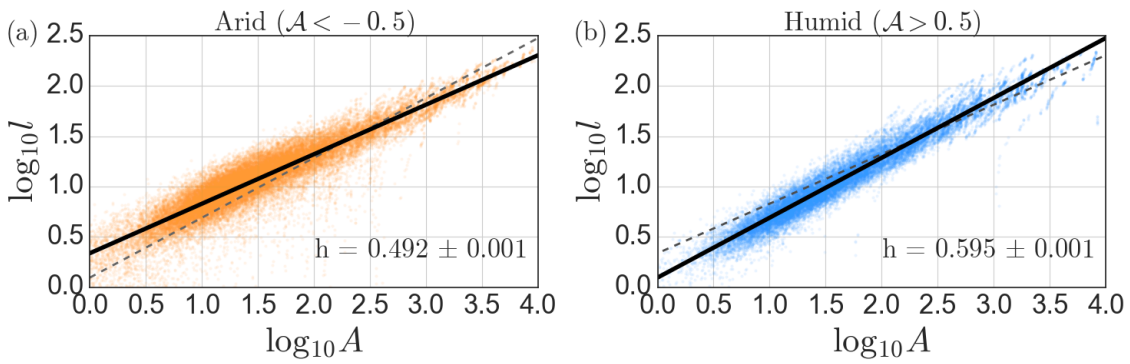

Figure 4-1: $\log_{10} l$ vs $\log_{10} a$ for (a) arid (orange, $\log_{10} \mathcal{A} < -0.5$) and (b) humid (blue, $\log_{10} \mathcal{A} > 0.5$) regions. The black straight lines are fit to the points shown by least squares regression, and correspond to Hack exponents of $h = 0.5$ for the arid data and 0.6 for the humid data. The dotted grey lines indicate fits to the points shown in the opposing plot, for reference. The axis limits in both plots are the same.

4.2 Results

4.2.1 Scaling, universality, and climate

River basin scaling is frequently characterized through a canonical scaling law known as Hack's law (Hack, 1957), which relates mainstream length l to basin area a by an exponent h, known as the Hack exponent:

$$l \sim a^h. \tag{4.1}$$

Following the analysis of branching angles in (Seybold et al., 2017), here we consider how an environmental gradient, namely aridity index, influences h. To this end, we calculate aridity index over the contiguous United States, defined as $\mathcal{A} = P/\text{PET}$ (Middleton and Thomas, 1992), where P is precipitation rate and PET is potential evapotranspiration. High values of $\mathcal{A}$ correspond to humid regions, while low values of $\mathcal{A}$ correspond to arid regions. This calculation is described further in the Methods section. We fit lines to data of $\log_{10} l$ against $\log_{10} a$ to obtain h for arid and humid basins, shown in figure 4-1. We find that arid basins have a Hack exponent of $h \simeq 0.5$, while humid basins have $h \simeq 0.6$, suggesting that the aridity index parameterizes the scaling exponent h.

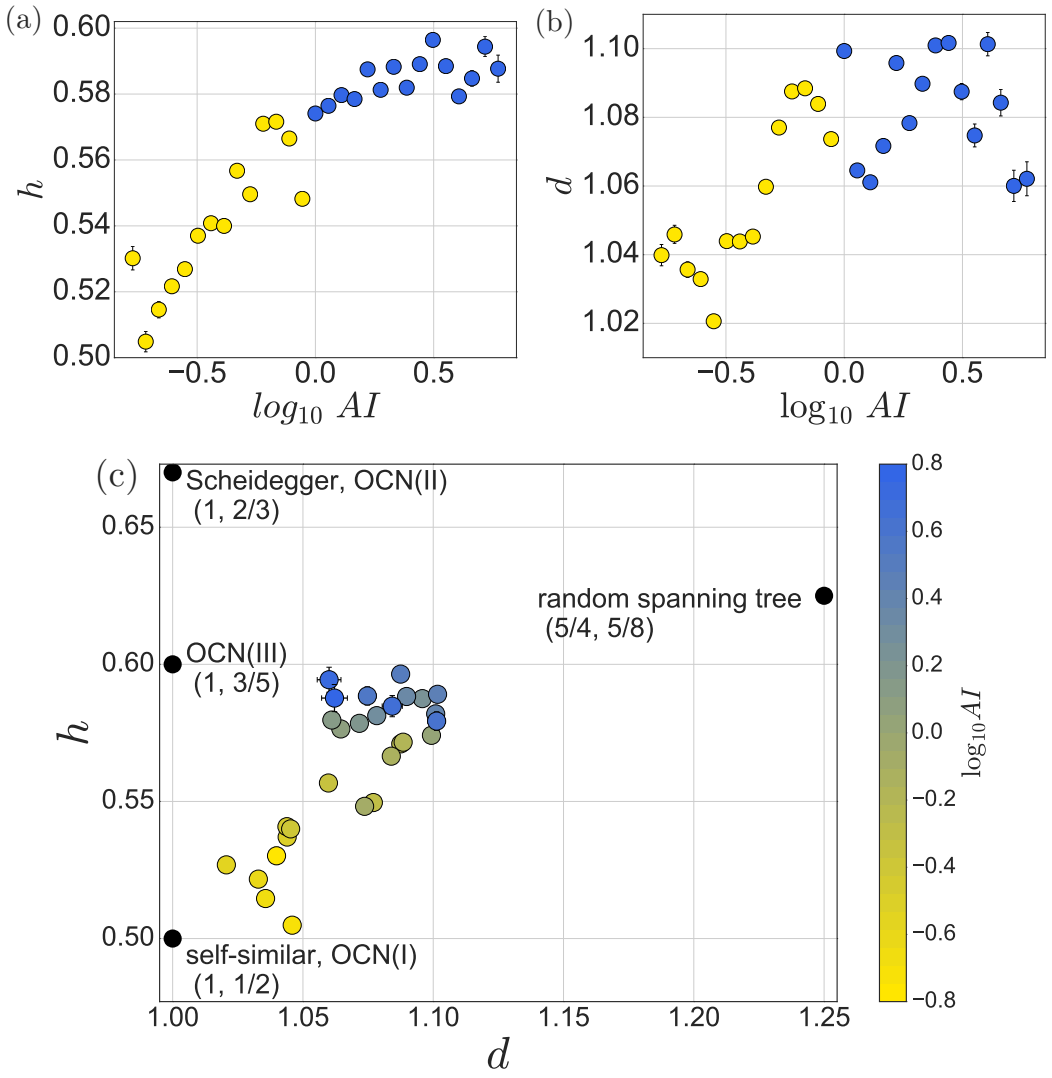

Figure 4-2: Behavior of (a) h ($l \sim a^h$) and (b) d ($l \sim L_{\|}^d$) as a function of aridity index. Error bars indication standard error. (c) Behavior of h and d, with different universality classes indicated.

Although Hack's law is canonically used to study how basin shape changes with scale, it alone does not provide a complete picture of river network scaling. We must also consider a law measuring the sinuosity of streams to fully define the basin shape and how it scales with size (Dodds and Rothman, 2000, 1999; Willemin, 2000):

$$l \sim L_{\|}^d, \tag{4.2}$$

where d is a scaling exponent. Together, d and h define a *universality class* of river

network (Dodds and Rothman, 2000, 1999), and adherence to a particular universality class would suggest that a river network's attributes can be largely understood through an underlying mathematical model.

The behaviors of d and h with $\mathcal{A}$ are shown in figure 4-2 (a) and (b). in figure 4-2 compares $d(\mathcal{A})$ and $h(\mathcal{A})$ to those predicted by simple mathematical models we referenced earlier (Dodds and Rothman, 2000). It appears that $(d, h) \simeq (1.04, 0.50)$ in arid environments and $(d, h) \simeq (1.09, 0.59)$ in more humid environments. These exponents suggest that river networks in arid environments are roughly self-similar, in that they do not change their proportions with changing scale (they also resemble one of the optimal channel networks), while those in humid environments are not, consistent with our observations in figure 4-5. Still, neither the arid nor humid basins bear a precise resemblance to these established universality classes of river networks.

4.2.2 Basin shape

The differences in Hack exponent for humid and arid basins should be manifested in the size-dependence of basin shape. We therefore explicitly consider basin shape to shed light on factors that may explain the scaling behavior we have observed. We define a basin width $L_\perp$, basin length $L_\parallel$, and basin area a. The aspect ratio $L_\perp/L_\parallel$ then defines the shape of a basin. Because $a \simeq L_\perp L_\parallel$, we can write this aspect ratio equivalently as $a/L_\parallel^2$, which we then calculate for all basins and sub-basins within the contiguous United States. A full explanation of these calculations can be found in the Methods. Figure 4-3(a) and (b) show maps of aridity index and $L_\perp/L_\parallel$ calculated in this way and assigned to the outlet of each sub-basin , and we find that the aspect ratio $L_\perp/L_\parallel$ indeed correlates with aridity, as shown in figure 4-3(c). In particular, basins in humid regions appear to be proportionally fatter than basins in arid regions.

To understand why, we consider how confluence angle can influence large-scale structure and consequently, basin shape. Consider a network that can be structurally approximated as a confluence branching symmetrically with an angle α between confluent branches off of a longer parent branch, as illustrated in figure 4-4. We can naturally draw a boundary between two branches, and thus between the two adja-

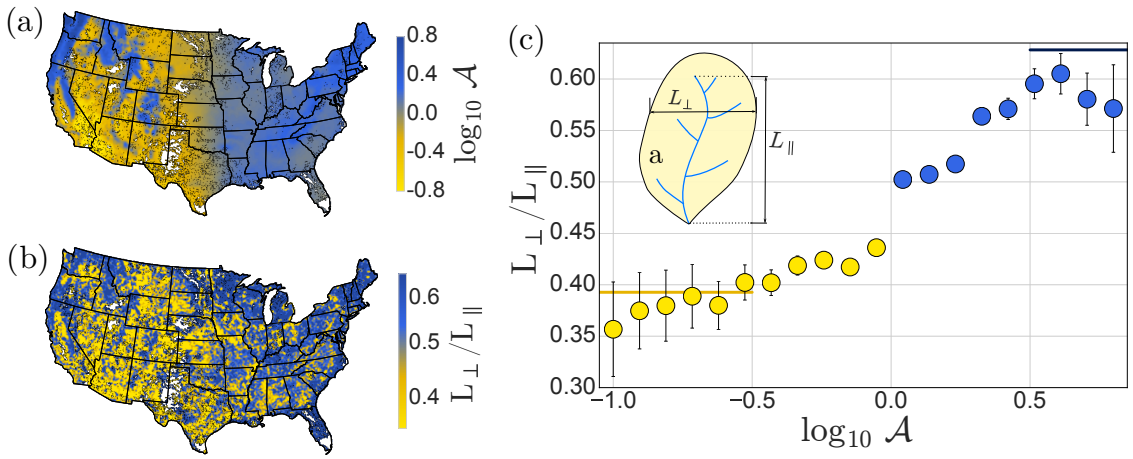

Figure 4-3: (a) Log aridity index $\log_{10} \mathcal{A}$ at the end-point of each sub-basin less than equal to Horton-Strahler order 4, interpolated over a grid over the contiguous United States. (b) Aspect ratio $L_\perp/L_\parallel$ at the end-point of each sub-basin less than or equal to Horton-Strahler order 4, interpolated over a grid over the contiguous United States. A smoothing filter over roughly 4 kilometers was applied to the data. Aspect ratio $L_\perp/L_\parallel$ as a function of $\log_{10} \mathcal{A}$, with error bars indicating standard error. The yellow solid line on the bottom left of the figure indicates $L_\perp/L_\parallel = \pi/8$ and the solid blue line in the upper right indicates $L_\perp/L_\parallel = \pi/5$.

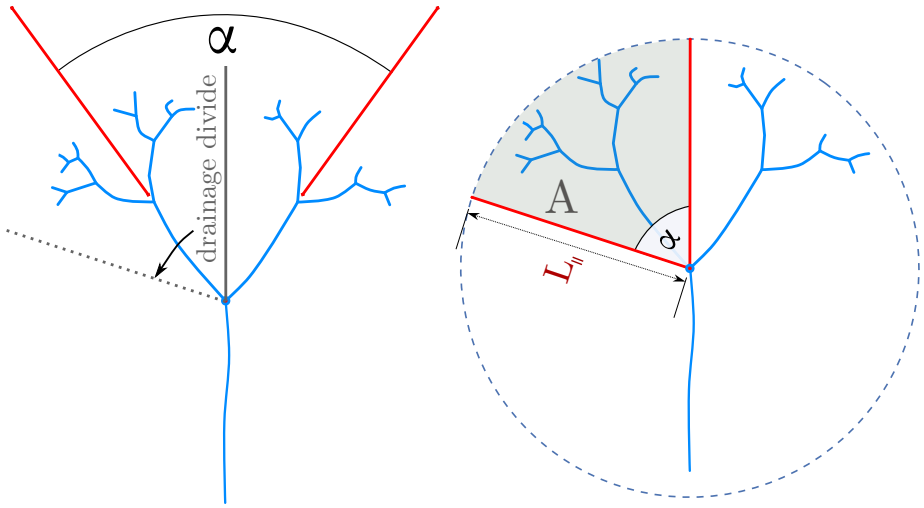

Figure 4-4: An illustration of how a confluence angle α might predict basin shape. If the basin is symmetric, the drainage basin can be delineated (left). If the network is then circumscribed within a circle, basin attributes can be defined as a function of branching angle (right).

cent basins, that is delineated by the direction of the parent channel. If we assume that these basins are symmetric (the area to the left of the stream is equal to the

area on the right), then it follows that the drainage area a of a basin of longitudinal extent $L_\parallel$ is simply a slice of angle α (radians) of a circle with radius $L_\parallel$:

$$a = \alpha L_\parallel^2 / 2. \tag{4.3}$$

Since $a \simeq L_\perp L_\parallel$, the aspect ratio

$$\frac{L_\perp}{L_\parallel} \simeq \frac{a}{L_\parallel^2} = \frac{\alpha}{2}. \tag{4.4}$$

Recent work has demonstrated that groundwater-fed channel networks grow in a direction that is determined by the shape of the surrounding groundwater table, predicting a branching angle of $2\pi/5 = 72°$ (Devauchelle et al., 2012; Cohen et al., 2015). And in an analysis of the contiguous United States, Seybold et al. (2017) find that this angle appears widespread in the local branching angles of humid environments, suggesting that the dynamics of groundwater processes may be influential in determining junction angle, while arid environments exhibit a narrower branching angle $\sim 45°$. If these two end-member branching angles represent network-wide structures, we can predict aspect ratios for this model network from the observed branching angles associated with humid and arid environments: a branching angle of $72°$ corresponds to $L_\perp/L_\parallel = \pi/5 \approx 0.63$, and a branching angle of $45°$ corresponds to $L_\perp/L_\parallel = \pi/8 \approx 0.39$. These values are indicated by solid blue and yellow lines in figure 4-3(c), respectively. The rough agreement suggests that the branching angles can naturally produce the observed changes in basin shape. This supports the idea that groundwater plays a substantial role in shaping river basins in humid environments.

To return to the question of variability in the Hack exponent, we consider how basin shape changes with scale. Figure 4-5 shows $L_\perp/L_\parallel$ as a function of basin area a for two different aridity ranges. We find that the aspect ratio in arid regions remains ~ 0.4 for basins of all sizes, indicating that arid basins proportions do not change with scale. However, the aspect ratio in humid regions indeed decreases as basin size increases, suggesting that their proportions do change with scale, in agreement with

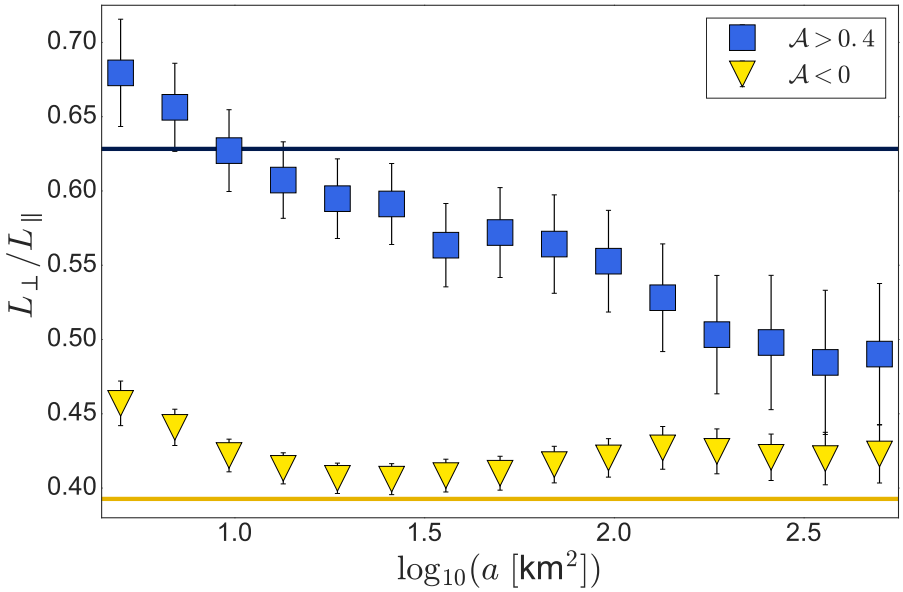

Figure 4-5: Dependence of aspect ratio $L_\perp/L_\parallel$ on a. Error bars indicate standard error.

our measurements of the basin scaling laws in figures 4-1 and 4-2. Specifically, humid basins appear to exhibit the $\pi/5 \approx 0.63$ aspect ratio when small, but as basin size increases, there is an apparent transition to the $\pi/8 \approx 0.39$ aspect ratio characteristic of arid basins.

4.3 Discussion

The Hack exponent of 0.5 found in arid basins is suggestive of a *self-similar* model of growth, suggesting that arid network proportions do not change with scale. The unchanging aspect ratio with basin area in figure 4-5 supports this hypothesis. However, humid basins do not exhibit such self-similarity. As humid basins become larger, they also become thinner, and their aspect ratio approaches that of arid basins, as shown in figure 4-5. This is consistent with a Hack exponent of $h \simeq 0.6$, but it is not obvious what processes are responsible for this behavior. To better understand this behavior, we more carefully consider humid basins.

First, we note that humid basins are more likely to have shallow groundwater tables, because of a high infliltration rate (Kirkby and Chorley, 1967; Bresciani et al.,

2016). Understanding how these groundwater tables influence river growth direction at different scales may therefore be important in understanding scaling properties in humid basins. Recent work suggests that these groundwater flows can predict growth direction, but the scale of this work was local, on the order of ~ 100 meters or less (Devauchelle et al., 2012; Cohen et al., 2015; Yi et al., 2017). We therefore ask how these local flows and their associated geometries can be contextualized within a larger groundwater system.

Toth (1963) introduced the notion of three different flow regimes: local, intermediate, and regional. On the local (and smallest) scale, groundwater fluxes do not generally have strong correlations to shape of the local topography, suggesting that the advance of their tips is dominated by local flows (Condon and Maxwell, 2015). This produces geometries (like the 72° branching angle) that can be understood through the groundwater field (Devauchelle et al., 2012; Yi et al., 2017). However, the regional scale (~ 144 km^2) exhibits a structure that appears to be tied to the topography, geology, and climate (Bresciani et al., 2016; Haitjema and Mitchell-Bruker, 2005; Devito et al., 2005). Over this scale, the exchange of flows between the distant streams can be interrupted by streams or reemerging groundwater "outcrops" between them. Depending on the height of the groundwater table and size of topographic undulations, groundwater flow may interact with the topography before reaching a stream, thereby complicating the flow field and effectively decoupling distant streams from each other.

The transition between these regimes is often characterized through a nondimensional number known as the water table ratio (Haitjema and Mitchell-Bruker, 2005; Condon and Maxwell, 2015):

$$\mathcal{W} = \frac{PL^2}{mkHd}, \tag{4.5}$$

where P is precipitation rate, k is the hydraulic conductivity, L is the distance between streams, m is a constant that describes the dimensionality of the flow, H is the thickness of the water table, and d is a distance between the highest topographic elevation and the elevation of the highest surface water feature. When $\mathcal{W} > 1$, the water table is considered "topography controlled": the water table rises close to the

surface, interacting with the topography. Conversely, when $\mathcal{W} < 1$, the water table is "recharge controlled": the water table is far from the surface, so rivers on this scale remain coupled through the groundwater table (Haitjema and Mitchell-Bruker, 2005).

We argue that the size-dependence of humid basin aspect ratio in figure 4-5 reflects the presence of a length scale L^* associated with this cutoff of $\mathcal{W}$. We contend that small, humid basins below this critical length (such that $\mathcal{W} < 1$) exhibit dynamics that reflect local groundwater flow, producing 72° junction angles and the corresponding wide basin aspect ratio. But as the basin increases in size, the ability of the largest branches to communicate with each other decreases, decoupling them and allowing for growth according to other processes. We can determine the critical characteristic length scale L^* by considering a calculation of water table ratio by Seybold et al. (2017), who calculate $\mathcal{W}$ and branching angle for a constant value of $L^2 = 100$ km^2. For this length scale, they find that the 72° branching angle corresponds to a value of $\mathcal{W} \sim 10^4$. If instead we leave L as a free parameter and ask what length scale corresponds to the cutoff $\mathcal{W} = 1$ for the 72° geometry, we find that $L^* \simeq 100$ meters. This suggests that 100 m is the limiting length scale beyond which groundwater streams no longer communicate.

This length scale agrees with the length scale of the smallest basins in figure 4-5 for which the humid aspect ratio holds, corresponding to a length scale of $\sim$ 100 m - 1 km. This agreement suggests that the $h \simeq 0.6$ scaling of humid basins reflects the decorrelation of the groundwater table as basin size increases. Beyond 100 m, other factors take hold. While we do not presume to know what these factors are, the convergence of the humid basin aspect ratio to the arid aspect ratio may indicate that large, humid basins self-organize in the same way that arid basins do (Rodríguez-Iturbe and Rinaldo, 2001; Howard, 1971a). Such a convergence may explain observations by Montgomery and Dietrich (1992) and others that suggest that large basins across varied climatic and geological conditions maintain their proportions with scale.

Our work suggests that humid river basins exhibit a unique, mathematical dichotomy. At the scale of large basins, arid and humid networks behave alike, col-

lecting water, perhaps doing so according to some optimal minimization scheme not unlike veins or trees (Dodds, 2010). Yet, on the scale of the tips, humid basins locally grow in response to a diffusive field, ramifying and dissecting the landscape in a quasistatic, geometrically elegant (Petroff et al., 2013) way. We expect that further work on the subject, particularly at higher resolution, may inform the intersection between hydrogeology, geomorphology, and physics.

4.4 Materials and methods

We study the geometry of drainage basins across the contiguous United States, derived from the NHD Plus Version 2 data set (McKay et al., 2012). Each drainage basin is comprised of a number of sub-basins, each with a total upstream drainage area a and mainstream length l. From the mainstream, we find the longitudinal basin length, $L_{\|}$, by taking the distance between the start and end coordinates of the longest channel. These start and end coordinates were obtained by projecting the NHDPlus stream networks onto the Lambert conformal cone 102004 projection as described in (Seybold et al., 2017). We calculate each of these exponents as a function of $\log_{10}$ aridity index by obtaining the slope of a line fit by least squares to $\log_{10} l$ against $\log_{10} a$. To determine the climatic dependence of these exponents, we calculate the aridity index $\mathcal{A} = P/\mathrm{PET}$ (Middleton and Thomas, 1992), computed at 4 km resolution using data from PRISM (PRISM Climate Group, 2012), as in Seybold et al. (2017), then interpolate these values at the points of each channel. P is the precipitation rate, and PET is the potential evapotranspiration. Within each sub-basin, we take the geometric mean of the $\mathcal{A}$ over the entire length of all rivers in the sub-basin. For the maps in figure 4-3(a) and (b), the basin-averaged $\mathcal{A}$ and $L_{\perp}/L_{\|}$ were plotted at the outlet of the basin. For the calculation of the network scaling exponents, we fit a line in log-log space to geographically diverse points which exhibited values of $\mathcal{A}$ within the plotted bin ranges.

Chapter 5

Lessons learned and persistent questions

We have studied three problems:

1. An elevation-dependent diffusivity can produce a valley edge which, in conjunction with a diffusive topography, can accurately predict the shape of slow-moving river valleys.

2. The balance of groundwater flux to valley sidewalls and confinement results in the lateral migration of streams, producing both a 120° opening angle in stream confluences and a network-wide curvature fluctuation.

3. Networks grown with a 72° branching angle naturally produce a basin aspect ratio (basin width to basin length) of $\pi/5$. Agreement of measured aspect ratios in humid regions to this value suggest that groundwater dynamics may influence large-scale basin shape. A study of scaling laws and allometry suggests that this effect may decrease with basin size.

These results offer some insight into how simple dynamics can translate to large scale behavior. First, our model of valley formation arose from two simple assumptions: topography diffuses, and this diffusivity varies. The variation in diffusivity gave rise to an effective jump condition which produced drastic changes in valley

shape. Second, our model of lateral rearrangement simply arises from the addition of a second diffusive field – the groundwater field. The addition of this second field gives rise to a statistical steady state that produces novel dynamics and features in the planform shape of groundwater-fed streams. Finally, we considered a tip-splitting network grown through the assumptions that basins are symmetric and exhibit a uniform branching angle, and found that junction-scale branching angles can influence basin shape over several orders.

However, as one might expect, some questions linger. Though some factors seem to survive renormalization, what happens to the other factors that appear so important on smaller scales? Why does the signature of groundwater on basin shape appear to disappear for large basins? Where happens to the influence of the topography in larger systems? Why do most meanders look so unlike the fluctuations in curvature we saw in chapter 3?

On the one hand, one can conjecture the geomorphological answers to these questions. As rivers and basins grow in size, they draw more flux, and the dynamics within the river interior likely grab hold of the system at some scale. This increased flux will scour river beds and form meanders, drive water in directions that thwart the 72° prediction, and ablate topographic signatures of slow growth. But perhaps an alternate answer lies in the metaphor I offered at the start of this journey – the drunkard. His reckless motion and collision will always produce beautiful shapes, but the shapes will change if you simply start him on a hill.

Appendix A

What does Laplacian growth tell us about river network statistics?

Abstract

A few things.

A.1 An overview

In Chapter 3, we discussed how the planform geometry of groundwater-fed channels can be largely attributed to the shape of the surrounding Laplacian field, particularly in the form of the $2\pi/5$ confluence angle (Devauchelle et al., 2012) and the idea that streams grow in a direction that satisfies local symmetry (Cohen et al., 2015). While recent work (Seybold et al., 2017) and Chapter 4 suggest that this understanding can be extended to humid environments in general, the explicit connection from groundwater dynamics to large-scale statistics has not been fully explored. While I do not claim to fully explore this connection here, in what follows, I will present several theoretical results that may shed light on how our understanding of growth in humid environments (i.e. growth in a Laplacian field) can change the way we interpret network statistics. In particular, I suggest that the distribution of first-order streams in primarily groundwater-fed environments gives a probability of tip-splitting as a

function of length, and that the ratio of sidebranch length distribution to confluence length distribution can predict the exponent of the stream power law. As is, the resolution of the national hydrological database is not sufficient to resolve the smallest streams, and the statistics do not appear cleanly for the limited data within our high-resolution network in Florida, but we will explore the aforementioned connections nonetheless, for posterity.

A.2 Flux as a function of branch length

We first present a relationship between flux and branch length in two familiar geometries – the "fishtail" (bifurcated stream) shape and the "sidebranch" shape. We will later use these results to deduce probability distributions for channel lengths.

A.2.1 Fishtail

Consider two conformal maps: $g(z)$ and $f(w)$. Let $g(z)$ denote the conformal maps from the growing tip (the physical plane) to the upper half plane (the mathematical plane), and let $f(w)$ denote its inverse map. Expansion of $g(z)$ around a point γ (corresponding to p in the upper half plane) yields

$$g(z) = p + \hat{a}_1\sqrt{z-\gamma} + \hat{a}_2(z-\gamma) + ... \tag{A.1}$$

If we let γ be the location of the spring, $a_1 = |\hat{a}_1|$ scales with flux into said spring (Petroff et al., 2013). However, because the inverse mapping $f(w)$ can often be found more readily through the use of Schwarz-Christoffel transformations, it is often useful to work with the inverse mapping $f(w)$ instead. Expansion of f around the tip $g(\gamma) = p$ gives

$$f(w) = f(p) + c_2(w-p)^2 + ... \tag{A.2}$$

The time-dependent fishtail map corresponds to the complex map shown in Figure 2-4

$$f(w) = w^{2/5}(5t - w^2)^{4/5}. \tag{A.3}$$

This function maps the upper half complex plane to a geometry where a stream of semi-infinite extent splits into two symmetric channels, as shown in Figure 3-11. The second derivative of this mapping is

$$f''(w) = -\frac{16w^{12/5}}{25(5t-w^2)^{6/5}} - \frac{72w^{2/5}}{25(5t-w^2)^{1/5}} - \frac{6(5t-w^2)^{4/5}}{25w^{8/5}}. \tag{A.4}$$

The second-order coefficient of this mapping at the pole $w = \sqrt{t}$ is thus

$$c_2 = \frac{f''(\sqrt{t})}{2} = -2^{3/5}. \tag{A.5}$$

We can relate c_2 to $\hat{a_1}$ in by comparing terms in equations (A.1) and (A.2). Relating this coefficient to $\hat{a}_1$, we find

$$\hat{a}_1 = -\frac{i}{2^{3/10}}. \tag{A.6}$$

And since $a_1 = |\hat{a}_1|$,

$$a_1 = 2^{-3/10} = \text{const.} \tag{A.7}$$

indicating that a_1 in this geometry is constant and therefore independent of time (and channel length).

This result is also not tied to the choice of branching angle. If instead we use the generalized mapping, $f(w) = w^{2c}(\frac{t}{c} - w^2)^{1-c}$, where $c = \frac{\alpha}{2\pi}$, and the tips of the function are located at $-\sqrt{t}$ and $\sqrt{t}$. Following the same procedure, we find the second-order expansion coefficient

$$c_2 = -2\left(\frac{1}{c} - 1\right)^{-c}, \tag{A.8}$$

which gives us

$$\hat{a}_1 = -\frac{i}{\sqrt{2}}\left(\frac{1}{c} - 1\right)^{c/2}, \tag{A.9}$$

and consequently,

$$a_1 = \frac{1}{\sqrt{2}}\left(\frac{1}{c} - 1\right)^{c/2}. \tag{A.10}$$

The tip length can be written as $l = f(\sqrt{t}) = t(\frac{1}{c} - 1)^{1-c} \sim t$. We again find there is

no dependence of a_1 on t.

A.2.2 Sidebranch

We can repeat this calculation for the sidebranch (a finite channel branching off of an infinite one). The sidebranch corresponds to a complex map

$$f(w) = \sqrt{w^2 - t}, \tag{A.11}$$

which maps the upper half complex plane onto the upper half complex plane with a slit along the imaginary axis removed. This map is shown in Figure A-1. The channel tip, highlighted in red, occurs at $f(0)$. Because the base of this tip is centered at the origin, the length of the channel is $l = |f(0)|$. The second derivative of this mapping is:

$$f''(w) = -\frac{w^2}{(w^2 - t)^{3/2}} + \frac{1}{\sqrt{w^2 - t}} \tag{A.12}$$

As before, at the pole $w = 0$, we find

$$c_2 = \frac{f''(0)}{2} = \frac{1}{2i\sqrt{t}}. \tag{A.13}$$

And because $c_2 = 1/\hat{a}_1^2$, we find a_1

$$\hat{a}_1 = t^{1/4} + it^{1/4}. \tag{A.14}$$

Since $a_1 = |\hat{a}_1|$,

$$a_1 = \sqrt{2}\ t^{1/4} \tag{A.15}$$

However, $l = f(0) \sim t^{1/2}$. Thus,

$$a_1 \sim l^{1/2}, \tag{A.16}$$

indicating that a_1 in this geometry is dependent on the length of the sidebranch.

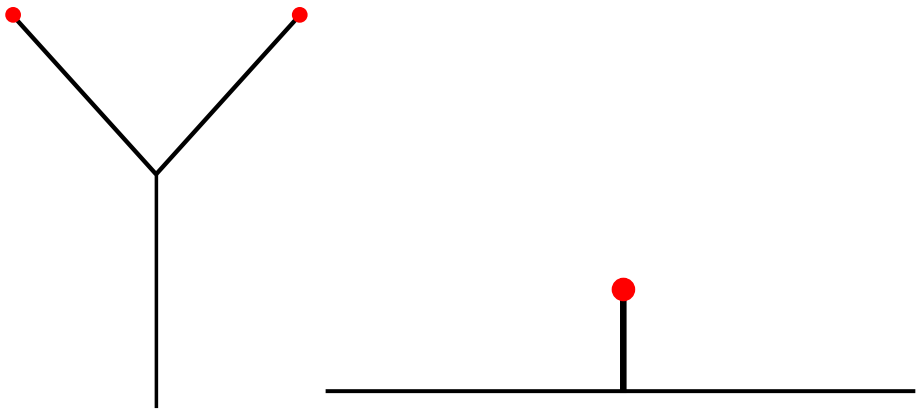

Figure A-1: An illustration of the physical planes of the conformal maps from the upper half plane to (a) the fishtail geometry of equation (A.3) to the sidebranch geometry of equation (A.11). The growing tip is shown in red. Unlabeled tips extend to infinity.

A.3 Length distributions

a_1 is therefore independent l for the fishtail geometry and dependent on l for the sidebranch geometry. A common assumption is that the rate of erosion (and thus the rate of stream advance) relates to the gradient of the groundwater field. That is,

$$v \sim |\nabla \phi|^{\eta} \sim a_1^{\eta} \tag{A.17}$$

This assumption has seen use in both problems of growth of singular Laplacian growth (Gubiec and Szymczak, 2008), as well as in problems of erosion mechanics as a stream power law (Whipple and Tucker, 1999). Recent work (Cohen et al., 2015) suggests that in a network of groundwater-fed channels in Bristol, Florida, $\eta \simeq 0.7$. But if this erosion law is true, we can combine them with equations (A.16) and (A.7) to obtain length distributions. As we have found, we can write a_1 as a function of stream length l

$$a_1 = F(l). \tag{A.18}$$

Substituting (A.18) into (A.17), we find

$$v \sim a_1^{\eta} = F(l)^{\eta}. \tag{A.19}$$

And therefore,

$$\frac{dl}{dt} = F(l)^{\eta}, \tag{A.20}$$

a differential equation which we can solve precisely for $l(t)$. Moreover, we can use Equation (A.20) to constrain the distribution of first-order channel lengths. Let $P(l)$ be the theoretical distribution of channel lengths and $P(t)$ the distribution of times for which these channels have existed.

$$P(t) = P(l(t))\frac{dl}{dt} \tag{A.21}$$

Let l_c refer to the lengths of channels that have grown primarily subject to the boundary conditions outlined by the fishtail geometry (we will henceforth call these "confluences"). Let l_s refer to the lengths of channels that have grown primarily subject to the boundary conditions outlined by the "sidebranch" geometry ("sidebranches"). Let the subscripts c and s denote references to confluences and sidebranches, respectively. We thus obtain two equations from equation A.21:

$$P_c(t) = P(l_c(t))\frac{dl_c}{dt} \sim P(l_c(t)), \tag{A.22}$$

$$P_s(t) = P(l_s(t))\frac{dl_s}{dt} \sim P(l_s(t))l^{\eta/2}. \tag{A.23}$$

We assume that streams have split more or less uniformly in time in recent history and therefore, that $P(t)$ is uniform. Simply, $P(t) \sim 1$. Therefore, we can rewrite (A.23) as:

$$P(l_c) \sim 1, \tag{A.24}$$

$$P(l_s) \sim l^{-\eta/2}. \tag{A.25}$$

Because real river networks do not grow infinitely in extent, their length distribution changes as channel tips split or new sidebranches form. Therefore $P(l)$ in equation (A.25) should be rewritten as subject to the condition that a channel has not yet branched, and similarly, a sidebranch has not formed along its length. We call this $P(l|\text{nb})$. We therefore apply Bayes' law to attempt to obtain $P(l)$ in terms of $P(l|\text{nb})$:

$$P(l) = P(l|\text{nb})P(\text{nb}) = P(l|\text{nb})(1 - P(\text{b})) \tag{A.26}$$

where $P(\text{b})$ denotes the probability of a branching event occurring at a certain length. Because $P(l_c|\text{nb}) \sim 1$, the real distribution of confluence lengths should then tell us precisely the value of $P(\text{nb})$:

$$P(l_c) = 1 - P(\text{b}). \tag{A.27}$$

Moreover, substitution of (A.26) into equation (A.25) gives us

$$\frac{P(l_c)}{P(l_s)} \sim l^{\eta/2} \tag{A.28}$$

Given a method for distinguishing channels that have grown as either confluences or sidebranches, we can then look at the shapes of these channel distributions and obtain an estimate of η and the probability of a tip-splitting event occurring for a given length.

A.4 Field observations

The simplest method of distinguishing these two types of channel is Horton-Strahler ordering — a stream-labeling scheme in which channels are designated by an 'order' n, indicating the presence of two order $n-1$ channels joining upstream Horton (1945); Strahler (1952). Under this labeling scheme, an actively growing spring is called a 'first-order' channel. When two first-order channels join, the downstream channel is called a second-order channel. Channels are part of a confluence when they join to form a higher-order stream, and a sidebranch if enter a higher-order stream down-

stream. We study first-order confluences and first-order sidebranches attached to second-order channels. Because we care about the initial growth conditions of the channels, for confluences (two first-order channels joining of lengths we denote l_1 and l_2, where $l_1 < l_2$), we label them as 'fishtail-like' if $l_1 > 0.8\ l_2$ and 'sidebranch-like' if $l_1 < 0.2\ l_2$. Similarly, for sidebranches, we label channels as 'sidebranch-like' if $l_1 < 0.2\ l$, where l is the maximal upstream length (the upstream second order length added to the length of the longer first-order channel attached to it).

A comparison of these two channel distributions for our field site is shown in Figure A-2, sorted according to the aforementioned method. A fit to these data gives $P(l_c) \sim l_c^{-1.69}$, and $P(l_s) \sim l_s^{-2.56}$, suggesting $\eta \simeq 1.74$. For this subset of the data, a Kolmogorov-Smirnow two-sample test rejects the null hypothesis that these are drawn from the same distribution with a p-value of 0.02.

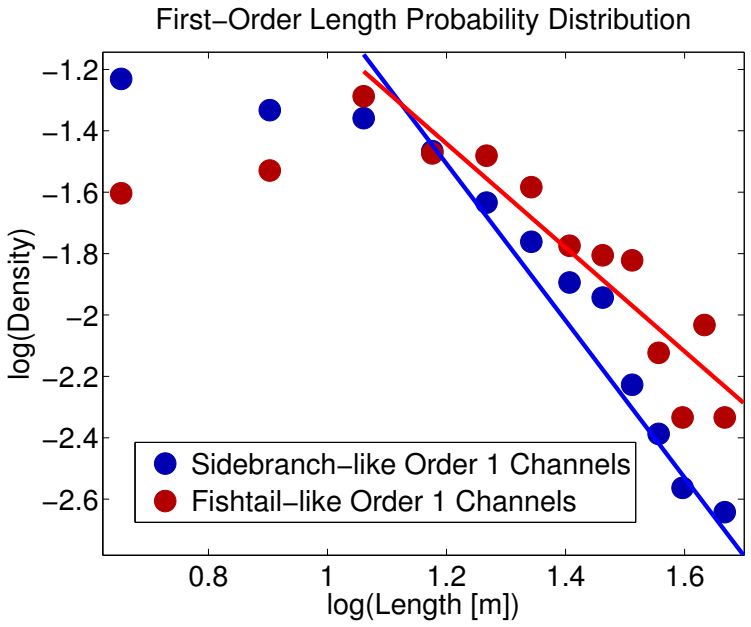

Figure A-2: First-order channel length distributions, separated into channels whose initial geometry is either more similar to either sidebranches and confluences. We ignore channels less than 10 meters long in our fit, reasoning that physical limitations prevent such short channels from splitting, and we also begin to reach the resolution of our data.

Bibliography

D.M. Abrams, A.E. Lobkovsky, A.P. Petroff, K.M. Straub, B. McElroy, D.C. Mohrig, A. Kudrolli, and D.H. Rothman. Growth laws for channel networks incised by groundwater flow. *Nature Geoscience*, 2(3):193–196, 2009.

P. Bak, C. Tang, and K. Wiesenfeld. Self-organized criticality: An explanation of the 1/f noise. *Physical review letters*, 59(4):381, 1987.

J. Bear. *Dynamics of Fluids in Porous Media*. 1972.

J.L. Best. Sediment transport and bed morphology at river channel confluences. *Sedimentology*, 35(3):481–498, 1988.

P.R. Bierman and D.R. Montgomery. *Key Concepts in Geomorphology*. W.H. Freeman, 2013.

E Bresciani, P Goderniaux, and O Batelaan. Hydrogeological controls of water table-land surface interactions. *Geophysical Research Letters*, 43(18):9653–9661, 2016.

C.J. Carey, T.G. Brown, K.C. Challis, A.J. Howard, and L. Cooper. Predictive modelling of multiperiod geoarchaeological resources at a river confluence: a case study from the Trent–Soar, UK. *Archaeological Prospection*, 13(4):241–250, 2006.

Y. Cohen and D.H. Rothman. Exact solution for the poisson field in a semi-infinite strip. In *Proc. R. Soc. A*, volume 473, page 20160908. The Royal Society, 2017.

Y. Cohen, O. Devauchelle, H.F. Seybold, R.S. Yi, P. Szymczak, and D.H. Rothman. Path selection in the growth of rivers. *Proceedings of the National Academy of Sciences*, 112(46):14132–14137, 2015.

L.E. Condon and R.M. Maxwell. Evaluating the relationship between topography and groundwater using outputs from a continental-scale integrated hydrology model. *Water Resources Research*, 51(8):6602–6621, 2015.

W.E.H. Culling. Analytical theory of erosion. *The Journal of Geology*, pages 336–344, 1960.

W.E.H. Culling. Soil creep and the development of hillside slopes. *The Journal of Geology*, pages 127–161, 1963.

W.E.H. Culling. Theory of erosion on soil-covered slopes. *The Journal of Geology*, 73(2):230–254, 1965.

L.J. Cummings, S.D. Howison, and J.R. King. Two-dimensional stokes and hele-shaw flows with free surfaces. *European Journal of Applied Mathematics*, 10(06):635–680, 1999.

H. Darcy. *Les fontaines publiques de la ville de Dijon: exposition et application...* Victor Dalmont, 1856.

O. Devauchelle, A.P. Petroff, A.E. Lobkovsky, and D.H. Rothman. Longitudinal profile of channels cut by springs. *Journal of Fluid Mechanics*, 667:38–47, 2010.

O. Devauchelle, A.P. Petroff, H.F. Seybold, and D.H. Rothman. Ramification of stream networks. pages 2–6, 2012. doi: 10.1073/pnas.1215218109.

O. Devauchelle, P. Szymczak, M. Pecelerowicz, Y. Cohen, H.F. Seybold, and D.H. Rothman. Laplacian networks: Growth, local symmetry, and shape optimization. *Physical Review E*, 95(3):033113, 2017.

K. Devito, I. Creed, T. Gan, C. Mendoza, R. Petrone, U. Silins, and B. Smerdon. A framework for broad-scale classification of hydrologic response units on the boreal plain: is topography the last thing to consider? *Hydrological processes*, 19(8): 1705–1714, 2005.

W.E. Dietrich, D.G. Bellugi, L.S. Sklar, J.D. Stock, A.M. Heimsath, and J.J. Roering. Geomorphic transport laws for predicting landscape form and dynamics. *Prediction in geomorphology*, pages 103–132, 2003.

P.S. Dodds. Optimal form of branching supply and collection networks. *Physical review letters*, 104(4):048702, 2010.

P.S. Dodds and D.H. Rothman. Unified view of scaling laws for river networks. *Physical Review E*, 59(5):4865, 1999.

P.S. Dodds and D.H. Rothman. Scaling, universality, and geomorphology. *Annual Review of Earth and Planetary Sciences*, 28(1):571–610, 2000.

T. Dunne. Hydrology, mechanics, and geomorphic implications of erosion by subsurface flow. *Special Paper-Geological Society of America*, (252):1–28, 1990.

J. Dupuit. *Etudes theoriques et pratiques sur le mouvement des eaux dans les canaux decouverts et a travers les terrains permeables avec des considerations relatives au regime des grandes eaux, au debouche a leur donner et a la marche des alluvions dans les rivieres a fond mobile*. Dunod, 1863.

A. Einstein. The cause of the formation of meanders in the courses of rivers and of the so-called baer's law. *Die Naturwissenschaften*, 14(11):223–224, 1926.

F. Engelund. Flow and bed topography in channel bends. *Journal of the Hydraulics Division*, 100(Proc. Paper 10963), 1974.

Y. Fan, H. Li, and G. Miguez-Macho. Global patterns of groundwater table depth. *Science*, 339(6122):940–943, 2013.

P. Forchheimer. Ueber die ergiebigkeit von brunnen-anlagen und sickerschlitzen. *Z. Architekt. Ing. Ver. Hannover*, 32:539–563, 1886.

T. Gubiec and P. Szymczak. Fingered growth in channel geometry: A Loewner-equation approach. *Physical Review E*, 77, 2008.

R.R. Gutierrez, J.D. Abad, M. Choi, and H. Montoro. Characterization of confluences in free meandering rivers of the amazon basin. *Geomorphology*, 220:1–14, 2014.

J.T. Hack. Studies of longitudinal stream profiles in virginia and maryland. Technical report, 1957.

H.M. Haitjema and S. Mitchell-Bruker. Are water tables a subdued replica of the topography? *Groundwater*, 43(6):781–786, 2005.

A.M. Heimsath, D.J. Furbish, and W.E. Dietrich. The illusion of diffusion: Field evidence for depth-dependent sediment transport. *Geology*, 33(12):949–952, 2005.

S. Herminghaus. Dynamics of wet granular matter. *Advances in Physics*, 54(3): 221–261, 2005.

E.J. Hickin and G.C. Nanson. Lateral migration rates of river bends. *Journal of Hydraulic Engineering*, 110(11):1557–1567, 1984.

J.M. Hooke. Changes in river meanders: a review of techniques and results of analyses. *Progress in Physical Geography*, 8(4):473–508, 1984.

R.E. Horton. Erosional development of streams and their drainage basins; hydrophysical approach to quantitative morphology. *Geological society of America bulletin*, 56(3):275–370, 1945.

M. Houssais, C.P. Ortiz, D.J. Durian, and D.J. Jerolmack. Onset of sediment transport is a continuous transition driven by fluid shear and granular creep. *Nature communications*, 6, 2015.

A.D. Howard. Optimal angles of stream junction: Geometric, stability to capture, and minimum power criteria. *Water Resources Research*, 7(4):863–873, 1971a.

A.D. Howard. Simulation model of stream capture. *Geological Society of America Bulletin*, 82(5):1355–1376, 1971b.

A.D. Howard and C.F. McLane. Erosion of cohesionless sediment by groundwater seepage. *Water Resources Research*, 24(10):1659–1674, 1988.

S.D. Howison. Complex variables in industrial mathematics. In *Proceedings of the Second European Symposium on Mathematics in Industry*, pages 153–166. Springer, 1988.

S.D. Howison and J.R. King. Explicit solutions to six free-boundary problems in fluid flow and diffusion. *IMA Journal of Applied Mathematics*, 42(2):155–175, 1989.

G.P. Ivantsov. The temperature field around a spherical, cylindrical, or pointed crystal growing in a cooling solution. In *Dokl. Akad. Nauk SSSR*, volume 58, pages 567–569, 1947.

L.P. Kadanoff, S.R. Nagel, L. Wu, and S. Zhou. Scaling and universality in avalanches. *Physical Review A*, 39(12):6524, 1989.

B.A. Kennedy. On Playfair's law of accordant junctions. *Earth Surface Processes and Landforms*, 9(2):153–173, 1984.

M.J. Kirkby and R.J. Chorley. Thoroughflow, overland flow and erosion. *International Association of Scientific Hydrology. Bulletin*, 12(3):5–21, 1967. doi: 10.1080/02626667709493533.

W. Kühnel. *Differential geometry*, volume 77. American Mathematical Soc., 2015.

L.B. Leopold and M.G. Wolman. River meanders. *Geological Society of America Bulletin*, 71(6):769–793, 1960.

S.S. Manna, D. Dhar, and S.N. Majumdar. Spanning trees in two dimensions. *Physical Review A*, 46(8):R4471, 1992.

A. Maritan, F. Colaiori, A. Flammini, M. Cieplak, and J.R. Banavar. Universality classes of optimal channel networks. *Science*, 272(5264):984, 1996.

L. McKay, T. Bondelid, T. Dewald, J. Johnston, R. Moore, and A. Rea. Nhdplus version 2: User guide, 2012.

N.J. Middleton and D.S. Thomas. World atlas of desertification. 1992.

D.R. Montgomery and W.E. Dietrich. Channel initiation and the problem of landscape scale. *Science*, 255(5046):826–830, 1992.

M.P. Mosley. An experimental study of channel confluences. *The journal of geology*, pages 535–562, 1976.

T.J. Nicoll and E.J. Hickin. Planform geometry and channel migration of confined meandering rivers on the canadian prairies. *Geomorphology*, 116(1):37–47, 2010.

S. Nowak, A. Samadani, and A. Kudrolli. Maximum angle of stability of a wet granular pile. *Nature Physics*, 1(1):50–52, 2005.

M.A. Palmer, E.S. Bernhardt, J.D. Allan, P.S. Lake, G. Alexander, S. Brooks, J. Carr, S. Clayton, C.N. Dahm, J. Follstad Shah, et al. Standards for ecologically successful river restoration. *Journal of applied ecology*, 42(2):208–217, 2005.

G. Parker. Surface-based bedload transport relation for gravel rivers. *Journal of hydraulic research*, 28(4):417–436, 1990.

J.D. Pelletier and J.T. Perron. Analytic solution for the morphology of a soil-mantled valley undergoing steady headward growth: Validation using case studies in southeastern Arizona. *Journal of Geophysical Research: Earth Surface*, 117(F2), 2012.

J.T. Perron, P.W. Richardson, K.L. Ferrier, and M. Lapôtre. The root of branching river networks. *Nature*, 492(7427):100–103, 2012.

E. Perucca, C. Camporeale, and L. Ridolfi. Influence of river meandering dynamics on riparian vegetation pattern formation. *Journal of Geophysical Research: Biogeosciences*, 111(G1), 2006.

A.P. Petroff, O. Devauchelle, D.M. Abrams, A.E. Lobkovsky, A. Kudrolli, and D.H. Rothman. Geometry of valley growth. *Journal of Fluid Mechanics*, 673:245–254, 2011.

A.P. Petroff, O. Devauchelle, A. Kudrolli, and D.H. Rothman. Four remarks on the growth of channel networks. *Comptes Rendus Geoscience*, 344(1):33–40, 2012.

A.P. Petroff, O. Devauchelle, H.F. Seybold, and D.H. Rothman. Bifurcation dynamics of natural drainage networks. *Philosophical Transactions of the Royal Society of London A: Mathematical, Physical and Engineering Sciences*, 371(2004):20120365, 2013.

P. Polubarinova-Kochina. Theory of ground water movement. *Princeton University Press*, 1962.

PRISM Climate Group. Oregon state university, 2012. URL `http://prism.oregonstate.edu`.

A. Rinaldo, I. Rodriguez-Iturbe, R. Rigon, E. Ijjasz-Vasquez, and R.L. Bras. Self-organized fractal river networks. *Physical Review Letters*, 70(6):822, 1993.

D.F. Ritter, R.C. Kochel, and J.R. Miller. *Process Geomorphology*. Waveland Press, Inc., 2011.

I. Rodrigeuz-Iturbe and A. Rinaldo. *Fractal River Basins: Chance and Self-Organization*. 1997.

I. Rodríguez-Iturbe and A. Rinaldo. *Fractal river basins: chance and self-organization*. Cambridge University Press, 2001.

J.J. Roering. Soil creep and convex-upward velocity profiles: Theoretical and experimental investigation of disturbance-driven sediment transport on hillslopes. *Earth Surface Processes and Landforms*, 29(13):1597–1612, 2004.

I.L. Rozovskii. *Flow of water in bends of open channels*. Academy of Sciences of the Ukrainian SSR, 1957.

P.G. Saffman and G. Taylor. The penetration of a fluid into a porous medium or Hele-Shaw cell containing a more viscous liquid. In *Proceedings of the Royal Society of London A: Mathematical, Physical and Engineering Sciences*, volume 245, pages 312–329. The Royal Society, 1958.

A.E. Scheidegger. A stochastic model for drainage patterns into an intramontane treinch. *Hydrological Sciences Journal*, 12(1):15–20, 1967.

S.A. Schumm, K.F. Boyd, C.G. Wolff, and W.J. Spitz. A ground-water sapping landscape in the Florida panhandle. *Geomorphology*, 12(4):281–297, 1995.

H.F. Seybold, D.H. Rothman, and J.W. Kirchner. Climate's watermark in the geometry of stream networks. *Geophysical Research Letters*, pages n/a–n/a, 2017. ISSN 1944-8007. doi: 10.1002/2016GL072089. URL `http://dx.doi.org/10.1002/2016GL072089`. 2016GL072089.

J.G. Speight. Meander spectra of the Angabunga River. *Journal of Hydrology*, 3(1): 1–15, 1965.

J. Stankiewicz and M.J. De Wit. Fractal river networks of southern africa. *South African Journal of Geology*, 108(3):333–344, 2005.

A.N. Strahler. Hypsometric (area-altitude) analysis of erosional topography. *Geological Society of America Bulletin*, 63(11):1117–1142, 1952.

D.G. Tarboton. A new method for the determination of flow directions and upslope areas in grid digital elevation models. *Water resources research*, 33(2):309–319, 1997.

D.G. Tarboton, R.L. Bras, and I. Rodriguez-Iturbe. The fractal nature of river networks. *Water Resources Research*, 24(8):1317–1322, 1988.

J. Toth. A theoretical analysis of groundwater flow in small drainage basins. *Journal of geophysical research*, 68(16):4795–4812, 1963.

M.G. Unde and S. Dhakal. Sediment characteristics at river confluences: a case study of the Mula-Kas confluence, Maharashtra, India. *Progress in Physical Geography*, 33(2):208–223, 2009.

E.W. Weisstein. Curvature. From MathWorld—A Wolfram Web Resource, 2017a. URL http://mathworld.wolfram.com/Curvature.html. Last visited on 2017-06-21.

E.W. Weisstein. Riemann mapping theorem. From MathWorld—A Wolfram Web Resource, 2017b. URL http://mathworld.wolfram.com/RiemannMappingTheorem.html. Last visited on 2017-06-25.

K.X. Whipple and G.E. Tucker. Dynamics of the stream-power river incision model: Implications for height limits of mountain ranges, landscape response timescales, and research needs. *Journal of Geophysical Research: Solid Earth*, 104(B8):17661–17674, 1999.

J.H. Willemin. Hack's law: Sinuosity, convexity, elongation. *Water resources research*, 36(11):3365–3374, 2000.

S.D. Willett, S.W. McCoy, J.T. Perron, L. Goren, and C.-Y. Chen. Dynamic reorganization of river basins. *Science*, 343(6175):1248765, 2014.

R.S. Yi, Y. Cohen, O. Devauchelle, R.G. Gibbins, H.J. Seybold, and D.H. Rothman. Symmetric rearrangement of groundwater-fed streams. *In review*, 2017.